ACTIVE FAULTING AND QUATERNARY SLIP RATES OF THE COLOMBIAN SUB-ANDES

by

Gabriel Eduardo Veloza-Fajardo
B.S., Universidad Nacional de Colombia, 2005

Submitted to the Department of Geology
and the Faculty of the Graduate School of
The University of Kansas in partial
fulfillment of the requirements for the
degree of Master of Science
2012

Advisory Committee

_____
Michael H. Taylor – Chair

_____
Douglas Walker

_____
Craig Marshall

Date Defended 10/10/12

The Thesis Committee for Gabriel Eduardo Veloza-Fajardo

certifies that this is the approved version of the following thesis

ACTIVE FAULTING AND QUATERNARY SLIP RATES OF THE COLOMBIAN SUB-ANDES

_____

Michael H. Taylor – Chair

_____

Douglas Walker

_____

Craig Marshall

Date Approved_____10/10/12_____

## ABSTRACT

Active deformation of northwestern South America is the result of the complex interaction between the Caribbean and Nazca plates subducting beneath South America, in sharp contrast to the classic Andean-type margin, south of 5° south latitude. This change in plate configuration is reflected in the distribution and kinematics of active structures in the upper plate, where strain is distributed over hundreds of active structures capable of generating damaging earthquakes. To achieve the goal of understanding the distribution and kinematics of active faults, digital archives of active structures are being compiled worldwide. These archives can be used in conjunction with many different tools (e.g. Global Positioning Systems) to estimate the modern slip rates of active faults, which in turn can be used by policy makers to determine better ways to build safer buildings.

As an example of recent deformation, and with the aim of comparing recent to millennial scale shortening rates, we analyze in detail the structural evolution of the Tame anticline, located in the Colombian sub-Andes. Here, we use detailed geomorphic and structural analysis from a 300 $km^2$ seismic survey to investigate the relationship between finite shortening and surface uplift and its effects on landscape evolution A quantitative description of finite shortening of the pre-growth strata from line-length and excess area calculations along the fold trend are presented and then compared, as an added check, with the uplift and shortening of geomorphic markers dated using in situ produced Terrestrial Cosmogenic Nuclides (TCN), providing the first estimates of Quaternary shortening along the Northern Colombian Andes at millennial time scales.

# ACKNOWLEDGMENTS

There are many people that have to be acknowledged for their support, one way or the other, for the completion of this degree. If I miss someone here, please excuse me. First, thanks to Valeria and Guadalupe for joining me during this journey, without them my entire life might have become senseless. I'm also indebted to Mike Taylor, his guidance, encouragement, and constant support helped in my scientific development. I also want to express my gratitude to my committee members, Doug Walker and Craig Marshall for their suggestions and help throughout this process, and in general to all the faculty members that shaped me as a geologist. Thanks also to Rafael, Olga, Julia and Luisa for their love and support from Colombia.

I am also thankful to my peers at KU, Richard Styron, Andrew McCallister, Maureen Logan, Tandis Bidgoli, Willy Ritasse, Jeff Oalman and so many people whom embraced me during these years in Kansas, and of course to my friends in Colombia, Pizzas, Pato, Daniel, David, Roscar and Cesar for their constant humor and long-lasting friendship. Tom Clifton and Greg Chmiel were tremendously helpful during the laboratory phase of the project.

Thanks to Andrés Mora, German Bayona and Mauricio Parra for their encouragement to pursue graduate school - there is no better model to follow than theirs. I'm especially thankful to Guillermo Hernandez and Wilson Gil for their help and sharing information from the Llanos Basin.

This research was funded by The University of Kansas and Ecopetrol-ICP, through the collaborative project "Cronología de la deformación en las Cuencas Subandinas".

# TABLE OF CONTENTS

# Open source archive of active faults for northwest South America

**Gabriel Veloza**[1#]

**Richard Styron**[1]

**Michael Taylor**[1]

**Andres Mora**[2]

[1]**Department of Geology**

**University of Kansas**

**Lawrence, KS 66045**

[2]**Ecopetrol, Instituto Colombiano del Petróleo, Bucaramanga, Colombia**

[#]**Email address: gveloza@ku.edu**

**Submitted to GSA Today. Published, October 2012**

## 1.1 ABSTRACT

We present a publicly-available data base of active structures for the Northern Andes based on the literature, our own field mapping, and interpretation of digital elevation models, earthquakes, and the regional velocity field obtained from Global Positioning System (GPS) studies. Active Tectonics of the Andes database (ATA v.1.0) is a digital archive of over 400 active faults available in a variety of digital formats for use by the scientific and teaching

communities. ATA v.1.0 is an open source archive that is updateable based on new results obtained by the scientific community, and should prove useful to scientists, teachers, policy makers, and the general population. We use ATA v.1.0 in combination with surface velocities from GPS to evaluate the regional kinematics of faulting in northwest South America (NWSA). In particular, we find the development of active strike-slip systems is controlled in part, by the degree of convergence obliquity between subducting oceanic plates and South America.

## 1.2 INTRODUCTION

Active deformation of NWSA is characterized by the interaction between the Caribbean and Nazca plates with the South American margin, which is in sharp contrast to the classic Andean convergent margin south of 5˚ S. This change in plate configuration is reflected in the distribution and kinematics of active structures in the upper plate, where strain is distributed over hundreds of active structures capable of generating damaging earthquakes. In the south, Peru is dominated by thrust faulting along the forearc and sub-Andean zones, largely in response to subduction, whereas left lateral strike-slip and normal faulting are characteristic of higher elevations, and the retroarc region to the east (Dalmayrac and Molnar, 1981; Dewey and Lamb, 1992; McNulty and Farber, 1998) (Figure 1.1). Ecuador's recent deformation is similarly partitioned between well-developed thrust systems and the Guayaquil-Algeciras right-lateral fault system (Figure 1.1). Colombia exhibits a more complex tectonic framework with subduction of the Caribbean and Nazca slabs beneath NWSA, and the arc collision of the Chocó-Panamá indenter (Farris et al., 2011). The northern margin of South America is also partitioned

between south-directed thrusting along the southern Merida Andes, which contrasts with high rates of dextral shear across the central and northern portions of the range (Figure 1.1) accommodating transpression across the Caribbean- South American plate boundary (Pindell et al., 2005).

The Andes have dense population centers, concentrated mostly in elevated regions of the Venezuelan and Colombian Andes, and along the Pacific coasts of Ecuador and Peru. A shared characteristic of these urban centers is their proximity to seismically active faults. For example, the cities of Bucaramanga and Santiago de Guayaquil lie adjacent to the Bucaramanga and Guayaquil-Algeciras faults, and major cities such as Lima are above an active subduction zone. Earthquake hazards are not limited to the well-described subduction zone settings - devastating earthquakes occur in continental settings where active structures are often smaller but shallower and close to population centers (e.g., England and Jackson, 2011); the recent earthquakes in New Zealand and China (e.g. Robinson et al., 2011) provide recent examples. To achieve the goal of understanding the distribution and kinematics of active faults, digital archives of active structures are being compiled worldwide. Attention has been paid to the Andes (e.g., Paris et al., 2003; Costa et al., 2006), and similar databases have been made for other orogens (e.g., Styron et al., 2010) and the western US (USGS, 2006). These databases are useful for understanding seismic hazard, and the dynamic mechanisms driving deformation.

We present a publicly-available database, Active Tectonics of the Andes (ATA v.1.0), comprising over 400 active faults from northeast Venezuela to southern Peru. These structures were mapped from our own field observations, interpretation of geologic maps, topography,

remote sensing data and earthquake seismicity from national databases of the geological surveys of Venezuela, Colombia, Ecuador, and Peru (Funvisis, Ingeominas, EPN and IGP, respectively). Faults names and kinematics are compiled from academic journals, and regional compilations. Faults were mapped at scales ranging from ~1:1,000,000 to 1:100,000 depending on the scale of the structure, the quality of remote sensing imagery, and accounting for uncertainties in fault kinematics. ATA v.1.0 is suitable for displaying with most GIS packages (e.g., ArcGIS), the Generic Mapping Tools (Wessel and Smith, 1996), and Google Earth. Where available, millennial and longer-term slip rates and references are included as metadata in the .shp and .kml formats. Users input is encouraged to contribute to or refine the database.

**1.3 TECTONIC SETTING**

Slip partitioning in the Northern Andes is highly dependent on the plate boundary configuration relative to the surface velocity field. Where convergence is orthogonal we generally expect to observe pure shear deformation (in map view), whereas in regions of oblique convergence, an element of simple shear deformation is expected. Orthogonal convergence between the Nazca and South American plates is restricted to the region near 6° S latitude, whereas the Caribbean plate is underthrusting obliquely below northern South America (Figure 1.1). To the north and south, rapid increases in convergence obliquity leads to the development of significant trench-parallel strike-slip faults (Dewey and Lamb, 1992) (Figure 1.1). Thrust faults bound the forearc and sub-Andean zones though their shortening rates and histories are largely unknown. The northern tectonic domain is characterized by the presence

of abundant volcanism and low magnitude earthquakes, whereas volcanism is virtually absent south of the Carnegie Ridge; seismic events are larger, but less frequent (Figure 1.4).

### 1.3.1 Northern Andean Domain (~5°S - 12°N)

North of the Talara bend, slip partitioning occurs along active thrust and dextral faults. The longest dextral fault in this area is the Guayaquil-Algeciras (GA) fault system (Figure 1.1a), extending ~2000 km from central Ecuador to southern Colombia. The GA fault is segmented based on changes in fault strike, forming contractional structures along restraining bends. The southernmost segment is the Guayaquil-Pallatanga fault, which is dominantly right-slip, but close to the trench it is associated with normal faulting in the Gulf of Guayaquil. Estimated extension rates for the Gulf of Guayaquil range from 2.5 to 9 mm/yr (Lavenu, 2006), with a right-lateral component estimated to be 3.8±0.9 mm/yr over the last 1.4 Ma (Lavenu et al., 1995). The La Victoria-Pisayambo segment is thrust dominated and occurs along the central fault segment located in the Ecuadorian hinterland (Figure 1.1). Here, the GA fault has a slip rate of 1.4±0.3 mm/yr (Lavenu et al., 1995). The northern strand of the GA fault system is defined by the Chingual-La Sofia right-slip fault, also known as the Cayambe-Afiladores-Sibundoy fault, with slip rates between 7±3 mm/yr over the last 37 kyr (Ego et al., 1996) and a Quaternary average of 11.9±7 mm/yr (Tibaldi et al., 2007). The fault system continues to the northeast where east-directed range-bounding thrust faults occur along the easternmost Colombian Andes (Figure 1.1). In Colombia the GA fault system is described in detail by Velandia et al. (2005), where recently active structures include synthetic and antithetic Riedel faults, pull apart basins, and releasing bends. Based on the maximum age of Quaternary offset

geomorphic features, the minimum slip rate for the GA fault system in Colombia is ~1.5 mm/yr (Chorowicz et al., 1996). Potentially, the GA fault system merges with the easternmost frontal thrust system of Colombia (i.e., the Cusiana – Yopal fault system) although a direct kinematic linkage is not documented (Costa et al., 2006, Velandia et al., 2005). However, the kinematic compatibility between the GA fault system and the Cusiana- Yopal fault system suggests the two are interacting. Furthermore, observations from seismic reflection profiles also suggest active deformation is transferred into the active foreland basin (Mora et al., 2010).

Other first order fault systems of the Colombian Andes include the northwest-striking Santa Marta-Bucaramanga fault system (SMB), which is a left-slip fault system, approximately 500 km in length (Figure 1.1). Its southeastern tip is located near the central portion of the Eastern Cordillera, and sits above the Bucaramanga seismic nest and is thought to be the surface response to slab collision (Taboada et al., 2000). Here, the SMB fault system splays in map pattern into an imbricate fan and links with northeast striking thrust faults (Figure 1.1). To the northwest, the SMB fault system terminates at the northwestern corner of the Sierra Nevada de Santa Marta. Slip rate estimates for the SMB fault system range from 0.2 mm/yr, based on maximum ages of Quaternary offset features (Paris et al., 2000) to 5 and 15 mm/yr based on paleoseismological studies close to its northern end (Diederix et al., 2009; Idarraga and Romero, 2010). The SMB fault system has a 6±2 mm/yr interseismic rate based on elastic dislocation modeling of GPS data (Trenkamp et al., 2002).

In the region of the Maracaibo block, the Merida Andes do not represent a typical Andean-type convergent margin - there is no active volcanism or deep earthquake seismicity, and the location and extent of the subducting slab remains uncertain (Figure 1.1a and 1.4) (van

der Hilst and Mann, 1994; Bezada et al, 2010). Active slip appears to be partitioned mainly between east-striking right-slip faults across Venezuela, and onto south-directed thrust systems associated with the South Merida thrust system. A significant structure of this kinematic domain is the right slip Boconó – Ancon – El Pilar fault system (BAP), which is ~1,600 km in length. The BAP fault system is east-striking and transfers slip from the subduction zone associated with the eastern Caribbean plate boundary. The BAP fault system continues west and curves to the south where it terminates in eastern Colombia, feeding slip into a southeast-directed imbricate thrust system (Figure 1.1a). Fault slip rate estimates for different segments of the fault yield a Quaternary average of 10 mm/yr, (Audemard et al., 2000). Shortening rates along the south-verging thrusts of the Merida Andes remain unknown, as are rates of normal faulting in eastern Venezuela. Northwest of the BAP, is the Oca-Ancon fault system (OA) which is a right lateral fault extending more than 400 km from Venezuela to northern Colombia where it bounds the northern margin of the Santa Marta massif, forming a v-shaped conjugate fault system with the SMB fault (Trenkamp et al., 2002; Acosta et al., 2007; Costa et al., 2006). Based on paleoseismological analysis, the OA fault system has a slip rate of ~2 mm/yr (Audemard, 1996).

### 1.3.2 Central Andean Domain (~5° S - 15°S)

The convergent margin of the Peruvian Andes is characterized by oblique subduction of the Nazca plate (McNulty et al., 1998), as well as the subduction of the Carnegie Ridge, Mendaña Fault Zone and Nazca Ridge at the northern, central and southern segments, with an inferred flat-slab geometry for the Nazca plate (Gutscher et al., 2000). The absence of seismicity

above the subducted Carnegie ridge and Mendaña Fault zone, combined with the absence of volcanism (Figures 1a and 2) is distinctive for this segment of the Peruvian Andes. Deformation in the Sub-Andean zone is accommodated by east-northeast directed thrusting in the eastern foothills, and interacting left-lateral and normal faults within the Andean highlands (Figure 1.1a).

Active thrust faults and folds are common along the sub-Andean zone of Peru. Plio-Pleistocene sediments are deformed by the west directed Campanquiz thrust on the eastern margin of the Santiago Basin (Figure 1.1a). Thrust faults are dominantly north-striking with lengths between 100-600 km, striking perpendicular to the main geodetic shortening direction. South of 5°S, the Andes change to a northwest trend. Here, left-lateral faults cut obliquely across the Andes from the retroarc foreland basin toward the Cordillera Blanca to the west. Estimated rates of strike-slip faulting range between 2-3 mm/yr over the last 2 Ma (Sebrier et al, 1985). The Cordillera Blanca is a west southwest-dipping detachment (normal) fault located in the Peru highlands, and is thought to represent either orogenic collapse (McNulty et al., 1998; Giovanni et al., 2010) or subduction of buoyant aseismic ridges-related extension (McNulty and Farber, 2002). Normal faults are also located along the Peru coast where offset marine terraces indicate slip rates of ~0.1 mm/yr. Here normal faulting accommodates coseismic subsidence in the landward part of the thrust wedge during strain release associated with subduction zone thrust events (Saillard et al., 2011).

**1.4 TECTONIC MODEL FOR ACTIVE DEFORMATION**

The ATA database is useful for synthesizing the regional tectonic framework, by comparing the distribution and kinematics of active faulting to the GPS velocity field (Figure 1.2). We compiled GPS velocities from a variety of sources (Kendrick et al., 2001; Perez et al., 2001; Trenkamp, et al., 2002; Perez et al., 2011; USGS, 2011), referenced to stable South America in the ITRF2000 reference frame. The velocities decrease eastward across the entire width of the orogen, consistent with previous studies using elastic dislocation modeling (e.g. Trenkamp et al., 2002) showing that convergence is primarily accommodated across the locked subduction megathrust with minor deformation accommodated on upper plate faults.

As described previously, high convergence obliquity leads to slip partitioned into thrusting along the trench and sub-Andes, and trench-parallel strike-slip faulting in the orogen interior. The GPS velocities are decomposed into their trench-normal and trench-parallel components (Figure 1.3); these surface velocities reflect end-member components of pure dip-slip faulting on thrust faults and horizontal motion along the strike-slip faults; the true degree of partitioning is not recoverable directly from the interseismic strain field, but earthquake focal mechanisms are consistent with active slip partitioning. Unlike previous studies, we consider the entire Andean margin north of southern Peru. In this view, the variation in convergence obliquity due to changing trend of the margin causes a large increase in the trench-parallel component of the velocity field, with the highest gradient of the velocity in southern Ecuador and northern Peru (Figure 1.1b). The large trench-parallel velocity gradient at the Talara bend suggests that trench-parallel extension is localized here, as indicated by northwest-striking normal faults at the Gulf of Guayaquil, where Pliocene sediments in the extensional basins exceed 5 km thickness (Lavenu et al., 1995). We suggest the trench-parallel

component of basal shear stresses acting on the North Andean block causes it to move in an arc-parallel direction due to oblique subduction (Figure 1.1b), analogous to the Sumatran arc (Fitch, 1972).

Although the northern Andes display a gross north-south symmetry at 5˚ S, differences between the Ecuadoran-Colombian and Peruvian Andes exists, observed both in the GPS velocity field and in the distribution of active faults (Figures 1 and 3). North of 5˚ S, the across-strike gradient in trench-parallel velocity is large, at 1-2 cm/yr of dextral shear. In the south, the trench-parallel velocity gradient is consistent with sinistral shear at < 1 cm/yr (Figure 1.3). Similarly, trench-parallel strike-slip faulting in Ecuador and Colombia is well-developed, with faults extending for 100's of kilometers and Holocene slip rates near 1 cm/yr (e.g. GA fault system – Lavenu et al., 1995; Tibaldi et al., 2007). Peruvian trench-parallel strike-slip faults, only observed in central and southern Peru, are shorter along-strike, suggesting less displacement magnitude (e.g. Cowie and Scholz, 1992) and possibly lower slip rates, but the rates are currently unknown. The differences may result in part from the different boundary conditions on the far end of mobile blocks. The North Andes override the Caribbean plate, resembling a subduction boundary in some respects, while motion of the southern coastal block is constrained by the Altiplano and northward-moving slivers south of the bend (Wang et al., 2007). Slip partitioning in Venezuela is largely reflected by right-slip faulting with slip rates between 3-17 mm/yr, (Figure 1.3) which is in agreement with seismological derived slip rates from seismological analysis of 8-10 mm/yr for the Boconó Fault (Audemard et al., 2000). In comparison, north-south shortening plays a more minor role, but is still significant with shortening rates of ~2 mm/yr (Figure 1.3).

## 1.5 CONCLUSIONS

The Ecuadoran-Colombian and Peruvian Andes display similar deformation styles, mirrored across latitude ~5˚S. Although a wide variety of factors such as rheology and mantle dynamics exert control on deformation (e.g. Isacks, 1988), which were not taken into account in this analysis, the observed slip partitioning is largely controlled by the local convergence velocity and degree of convergence obliquity. In the north, convergence is highly oblique and slip partitioning is expressed as trench-normal thrusting and rapid and well-developed trench-parallel right-slip faulting as shown in the upper part of Figure 1.3b. This region is also characterized by abundant, but low-magnitude earthquakes (Figure 1.4) and active volcanism between 5˚ S and 7˚ N, where the subducting slab is inferred to dip ~30˚ (Gutscher et al., 2000; Figure 1.2). The subduction geometry is thought to change near the active arc collision with the Chocó-Panamá block, where flat slab subduction shifts volcanism to eastern Colombia (Figures 1 and 2).

Large gradients in trench-parallel motion may cause extension in the Gulf of Guayaquil. To the south, in northern Peru, convergence obliquity is relatively low and trench-parallel left-slip faulting is not observed. However, the trench-parallel component of the surface velocity field increases to the south, commensurate with increasing convergence obliquity. Pure shear deformation of the central Andes is expressed as active east-directed shortening and crustal thickening, while strike slip faulting and eastward transport occurs to the north. Right slip faulting is characteristic of the Merida Andes, accommodating the eastward motion of the Caribbean plate and the limited coupling across the plate boundary between South America and the Caribbean (Figure 1.1b).

## 1.6 ACTIVE TECTONICS OF THE ANDES DATABASE

The ATA-1.0 database may be downloaded at the following link: https://documents.ku.edu/ORGS/Academics/College of Liberal Arts and Sciences/Geology/ActiveAndesMap/ATA-1.0. For additions or modifications to the database, please contact the authors.


## ACKNOWLEDGEMENTS

Support for this work is through a collaborative grant between Ecopetrol-ICP project "Cronología de la deformación en las Cuencas Subandinas" and the University of Kansas. We thank Jeffrey Freymueller for valuable comments and discussions that improved and clarified our ideas. Comments and suggestions from two anonymous reviewers also improved the document.


## REFERENCES


- Acosta, J., Velandia, F., Osorio, J., Lonergan, L., and Mora, H., 2007, Strike-slip deformation within the Colombian Andes: Geological Society, London, Special Publications, v. 272, no. 1, p. 303-319.

- Audemard, F. A., Machette, M., Cox, J., Dart, R., and Haller, K., 2000, Map and Database of Quaternary Faults and Folds in Venezuela and its Offshore Regions, in USGS, ed., Open-File report 00-0018.
- Audemard, F. A. M., 1996, Paleoseismicity studies on the Oca-Ancón fault system, northwestern Venezuela: Tectonophysics, v. 259, no. 1-3, p. 67-80.
- Bezada, M., Magnani, M., Zelt, C., Schmitz, M., and Levander, A., 2010, The Caribbean–South American plate boundary at 65° W: Results from wide-angle seismic data: Journal of Geophysical Research, v. 115, no. B8, p. B08402.
- Chorowicz, J., Chotin, P., and Guillande, R., 1996, The Garzon fault: active southwestern boundary of the Caribbean plate in Colombia: Geologische Rundschau, v. 85, no. 1, p. 172-179.
- Costa, C., Audemard, F., Bezerra, H., Lavenu, A., Machette, M., and Paris, G., 2006, An overview of the main Quaternary deformation of South America: Revista de la Asociación Geológica Argentina, v. 61, no. 4, p. 461-479.
- Cowie, P. A., and Scholz, C. H., 1992, Displacement-length scaling relationship for faults: data synthesis and discussion: Journal of structural geology, v. 14, no. 10, p. 1149-1156.
- Dalmayrac, B., and Molnar, P., 1981, Parallel thrust and normal faulting in Peru and constraints on the state of stress: Earth and Planetary Science Letters, v. 55, no. 3, p. 473-481.
- Dewey, J., and Lamb, S., 1992, Active tectonics of the Andes: Tectonophysics, v. 205, no. 1-3, p. 79-95.

- Diederix, H., Hernandez, C., Torres, E., Osorio, J. A., and Botero, P., 2009, Resultados preliminares del primer estudio paleosismológico a lo largo de la Falla de Bucaramanga, XII Congreso Colombiano de Geología, Volume 1: Colombia.
- Ego, F., Sébrier, M., Lavenu, A., Yepes, H., and Egues, A., 1996, Quaternary state of stress in the Northern Andes and the restraining bend model for the Ecuadorian Andes: Tectonophysics, v. 259, no. 1-3, p. 101-116.
- England, P., and Jackson, J., 2011, Uncharted seismic risk: Nature Geoscience, v. 4, no. 6, p. 348-349.
- EPN, 2010, Catálogo de sismicidad 1990-2010, in Instituto Geofísico Escuela Politécnica Nacional, E., ed.: www.igepn.edu.ec.
- Farris, D. W., Jaramillo, C., Bayona, G., Restrepo-Moreno, S. A., Montes, C., Cardona, A., Mora, A., Speakman, R. J., Glascock, M. D., and Valencia, V., 2011, Fracturing of the Panamanian Isthmus during initial collision with South America: Geology, v. 39, no. 11, p. 1007-1010.
- Fitch, T. J., 1972, Plate convergence, transcurrent faults, and internal deformation adjacent to southeast Asia and the western Pacific: Journal of Geophysical Research, v. 77, no. 23, p. 4432-4460.
- FUNVISIS, 2011, Catálogo de sismicidad 2007-2011, in Sismológicas, F. V. d. I., ed.: http://www.funvisis.gob.ve.
- Giovanni, M. K., Horton, B. K., Garzione, C. N., McNulty, B., and Grove, M., 2010, Extensional basin evolution in the Cordillera Blanca, Peru: Stratigraphic and isotopic

records of detachment faulting and orogenic collapse in the Andean hinterland: Tectonics, v. 29, no. 6, p. TC6007.

- Gutscher, M. A., Spakman, W., Bijwaard, H., and Engdahl, E. R., 2000, Geodynamics of flat subduction: Seismicity and tomographic constraints from the Andean margin: Tectonics, v. 19, no. 5, p. 814-833.
- Idárraga-García, J., and Romero, J., 2010, Neotectonic study of the Santa Marta Fault System, Western foothills of the Sierra Nevada de Santa Marta, Colombia: Journal of South American Earth Sciences, v. 29, no. 4, p. 849-860.
- IGP, 2005, Catálogo sísmico Nacional 1985-2005, in Perú, I. G. d., ed.: http://www.igp.gob.pe
- INGEOMINAS, 2010, Catálogo sísmico nacional, 1993-2010, in Minería, I. C. d. G. y., ed.: www.ingeominas.gov.co.
- Isacks, B. L., 1988, Uplift of the central Andean plateau and bending of the Bolivian orocline: Journal of Geophysical Research, v. 93, no. B4, p. 3211-3231.
- Kendrick, E., Bevis, M., Smalley, R., and Brooks, B., 2001, An integrated crustal velocity field for the central Andes: Geochem. Geophys. Geosyst, v. 2, no. 11, p. 1066.
- Lavenu, A., 2006, Neotectónica de los Andes entre 1 N y 47 S (Ecuador, Bolivia y Chile): una revisión: Revista de la Asociación Geológica Argentina, v. 61, no. 4, p. 504-524.
- Lavenu, A., Winter, T., and Dávila, F., 1995, A Pliocene–Quaternary compressional basin in the Interandean Depression, Central Ecuador: Geophysical Journal International, v. 121, no. 1, p. 279-300.

- McNulty, B., and Farber, D., 2002, Active detachment faulting above the Peruvian flat slab: Geology, v. 30, no. 6, p. 567-570.
- McNulty, B. A., Farber, D. L., Wallace, G. S., Lopez, R., and Palacios, O., 1998, Role of plate kinematics and plate-slip-vector partitioning in continental magmatic arcs: Evidence from the Cordillera Blanca, Peru: Geology, v. 26, no. 9, p. 827-830.
- Mora, A., Parra, M., Strecker, M. R., Sobel, E. R., Zeilinger, G., Jaramillo, C., Da Silva, S. F., and Blanco, M., 2010, The eastern foothills of the Eastern Cordillera of Colombia: An example of multiple factors controlling structural styles and active tectonics: Geological Society of America Bulletin, v. 122, no. 11-12, p. 1846-1864.
- Paris, G., Machette, M. N., Dart, R. L., and Haller, K. M., 2000, Map and database of Quaternary faults and folds in Colombia and its offshore regions. , in USGS, ed., Open-File Report 00-0284.
- Pérez, O. J., Bilham, R., Bendick, R., Velandia, J. R., Hernández, N., Moncayo, C., Hoyer, M., and Kozuch, M., 2001, Velocity field across the southern Caribbean plate boundary and estimates of Caribbean/South-American plate motion using GPS geodesy 1994-2000 (Paper 2001GL013183): Geophysical Research Letters, v. 28, no. 15, p. 2987-2990.
- Pérez, O. J., Bilham, R., Sequera, M., Molina, L., Gavotti, P., Moncayo, C., Rodríguez, C., Guzmán, M., Codallo, H., and Velandia, R., 2011, Campo de velocidades GPS en el occidente de Venezuela: componente lateral derecha asociada a la Falla de Boconó y componente convergente perpendicular a Los Andes: Interciencia, no. 1, p. 39-44.
- Pindell, J., Kennan, L., Maresch, W. V., Stanek, K., Draper, G., and Higgs, R., 2005, Plate-kinematics and crustal dynamics of circum-Caribbean arc-continent interactions:

Tectonic controls on basin development in Proto-Caribbean margins: SPECIAL PAPERS-GEOLOGICAL SOCIETY OF AMERICA, v. 394, p. 7.

- Robinson, R., Van Dissen, R., and Litchfield, N., 2011, Using synthetic seismicity to evaluate seismic hazard in the Wellington region, New Zealand: Geophysical Journal International.
- Saillard, M., Hall, S., Audin, L., Farber, D., Regard, V., and Hérail, G., 2011, Andean coastal uplift and active tectonics in southern Peru: 10Be surface exposure dating of differentially uplifted marine terrace sequences (San Juan de Marcona,~ 15.4 S): Geomorphology.
- Sébrier, M., Mercier, J. L., Mégard, F., Laubacher, G., and Carey-Gailhardis, E., 1985, Quaternary normal and reverse faulting and the state of stress in the central Andes of south Peru: Tectonics, v. 4, no. 7, p. 739-780.
- Styron, R., Taylor, M., and Okoronkwo, M., 2012, Database of active structures from the Indo-Asian Collision: Eos Trans. AGU, v. 91, no. 20.
- Taboada, A., Rivera, L. A., Fuenzalida, A., Cisternas, A., Philip, H., Bijwaard, H., Olaya, J., and Rivera, C., 2000, Geodynamics of the northern Andes: Subductions and intracontinental deformation (Colombia): Tectonics, v. 19, no. 5, p. 787-813.
- Tibaldi, A., Rovida, A., and Corazzato, C., 2007, Late Quaternary kinematics, slip-rate and segmentation of a major Cordillera-parallel transcurrent fault: The Cayambe-Afiladores-Sibundoy system, NW South America: Journal of structural geology, v. 29, no. 4, p. 664-680.

- Trenkamp, R., Kellogg, J. N., Freymueller, J. T., and Mora, H. P., 2002, Wide plate margin deformation, southern Central America and northwestern South America, CASA GPS observations: Journal of South American Earth Sciences, v. 15, no. 2, p. 157-171.
- USGS, 2006, Quaternary fault and fold database for the United States, in USGS, ed.: http//earthquake.usgs.gov/regional/qfaults/.
- USGS, 2012, GPS Velocities Ecuador, in USGS, ed.: http://earthquake.usgs.gov/monitoring/gps/Ecuador/velocities/.
- van der Hilst, R., and Mann, P., 1994, Tectonic implications of tomographic images of subducted lithosphere beneath northwestern South America: Geology, v. 22, no. 5, p. 451-454.
- Velandia, F., Acosta, J., Terraza, R., and Villegas, H., 2005, The current tectonic motion of the Northern Andes along the Algeciras Fault System in SW Colombia: Tectonophysics, v. 399, no. 1, p. 313-329.
- Wang, K., Hu, Y., Bevis, M., Kendrick, E., Smalley Jr, R., Vargas, R. B., and Lauría, E., 2007, Crustal motion in the zone of the 1960 Chile earthquake: Detangling earthquake-cycle deformation and forearc-sliver translation: Geochemistry Geophysics Geosystems, v. 8, no. 10, p. Q10010.
- Wessel, P., and Smith, W. H. F., 1998, New, improved version of Generic Mapping Tools released: EOS transactions, v. 79, p. 579-579.

**FIGURES**

**Figure 1.1**

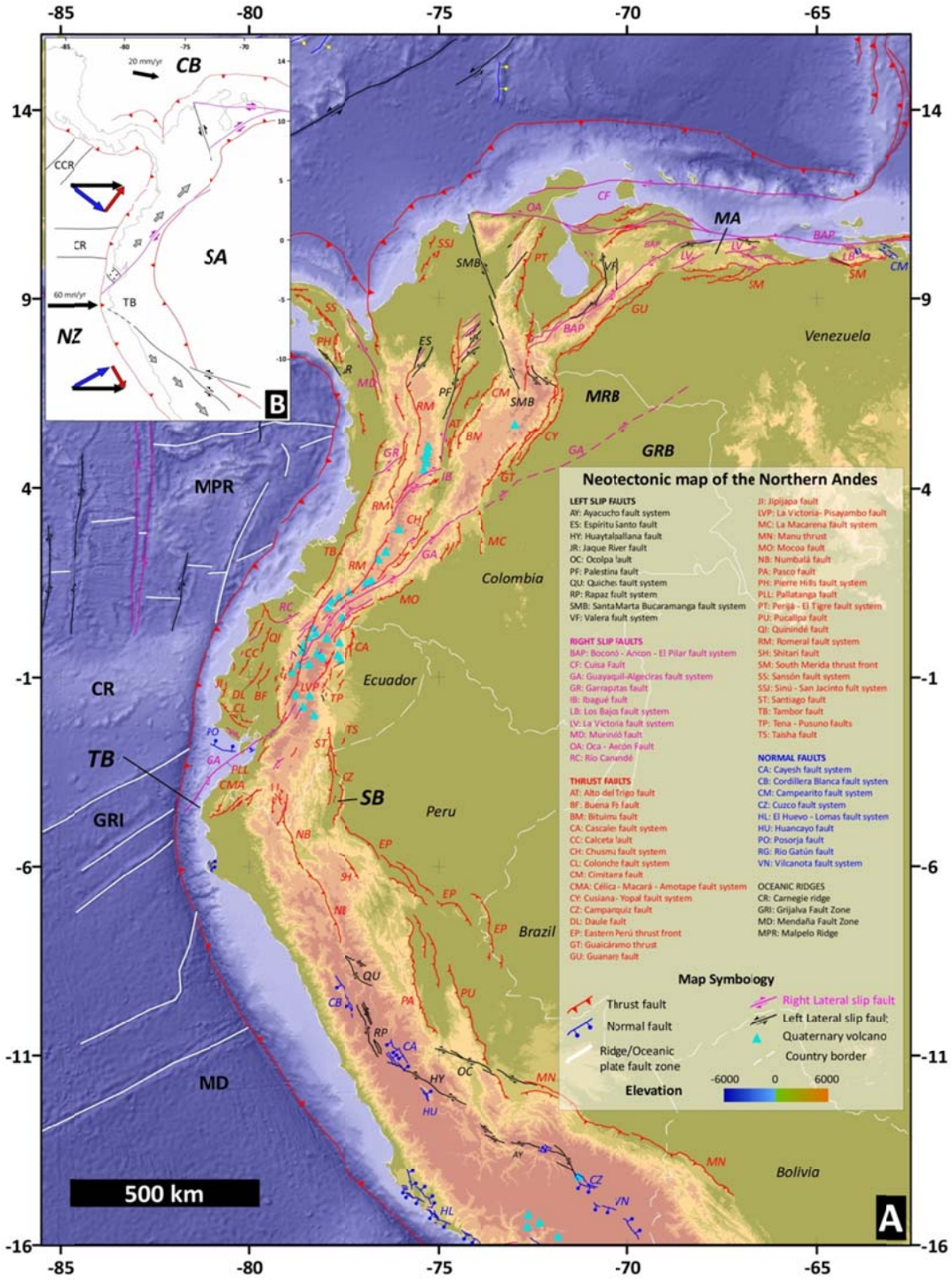

**Figure 1.1 (a)** Active faults of northwestern South America. Thrust faults and normal faults have barbs and balls on the hanging wall. Arrows indicate horizontal motion for strike slip faults. MA: Mérida Andes. TB: Talara Bend. SB: Santiago Basin. MRB: Meta River basin. GRB: Guaviare River basin. **(b)** Schematic model for slip partitioning of NWSA. Eastward motion of Nazca Plate is partitioned into trench-parallel (red arrows) and trench-normal (blue arrows) components. Velocities for Nazca and Caribbean Pates from Trenkamp et al. (2002). Trench-parallel components of the velocity field increase away from the TB, with the maximum velocity gradient located in that area. Note the position of the Carnegie Ridge relative to the TB, where strike-slip faults initiate. SA: South American Plate. NZ: Nazca Plate. CB: Caribbean Plate. CCR: Cocos Ridge.

**Figure 1.2**

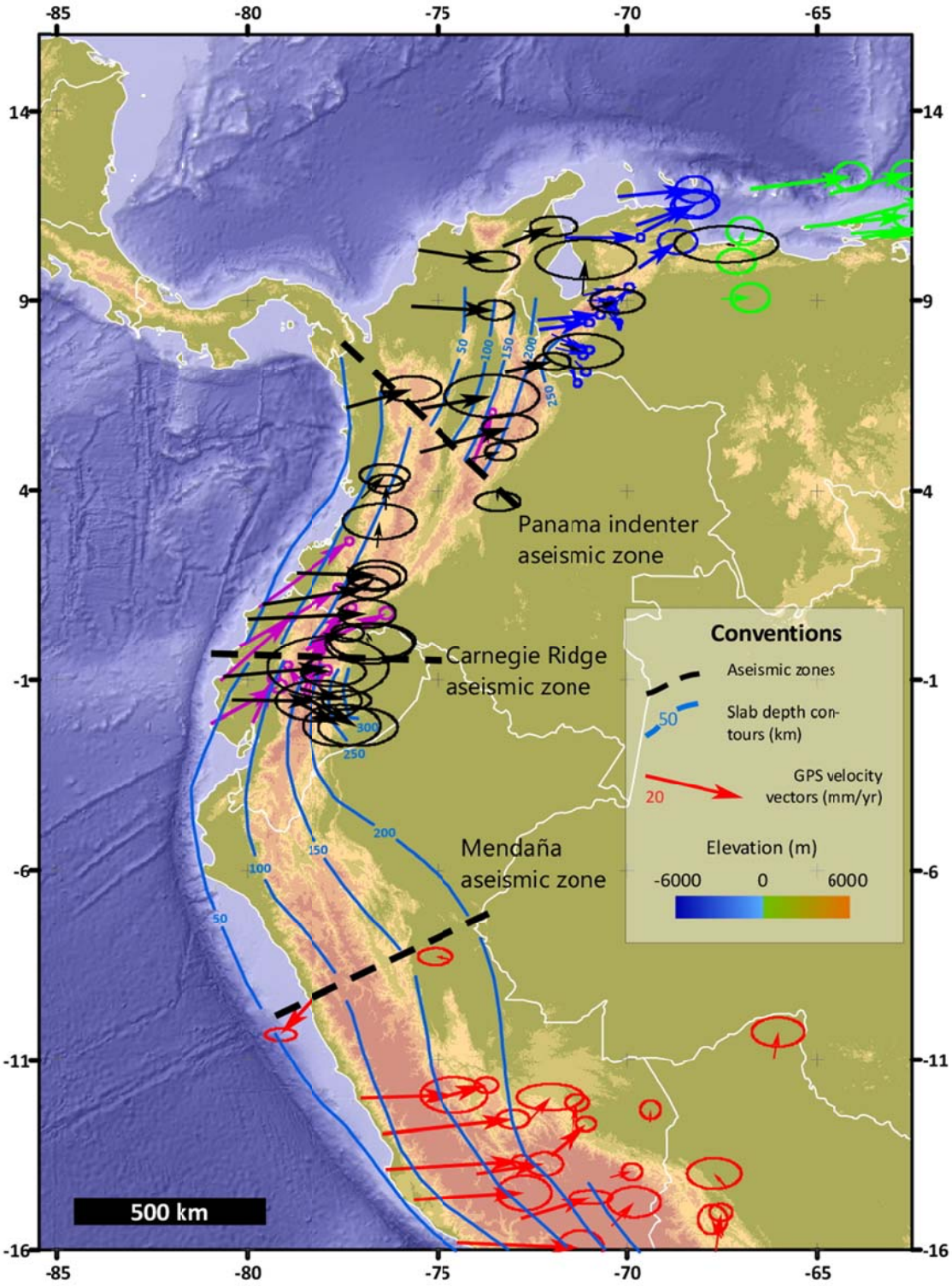
-85
-80
-75
-70
-65
14
9
4
-1
-6
-11
-16
Panama indenter
aseismic zone
Carnegie Ridge
aseismic zone
Mendaña
aseismic zone
Conventions
Aseismic zones
Slab depth contours (km)
GPS velocity vectors (mm/yr)
20
Elevation (m)
-6000
0
6000
500 km

**Figure 1.2** GPS velocity vectors for the Northern Andes from Kendrick et al., 2001 (red); Perez et al., 2001 (green); Trenkamp et al., 2002 (black); Perez et al., 2011 (blue) and the USGS, 2011 (purple). Structural contours for the Nazca slab determined from earthquake hypocenters, modified after Gutscher et al., (2000).

**Figure 1.3**

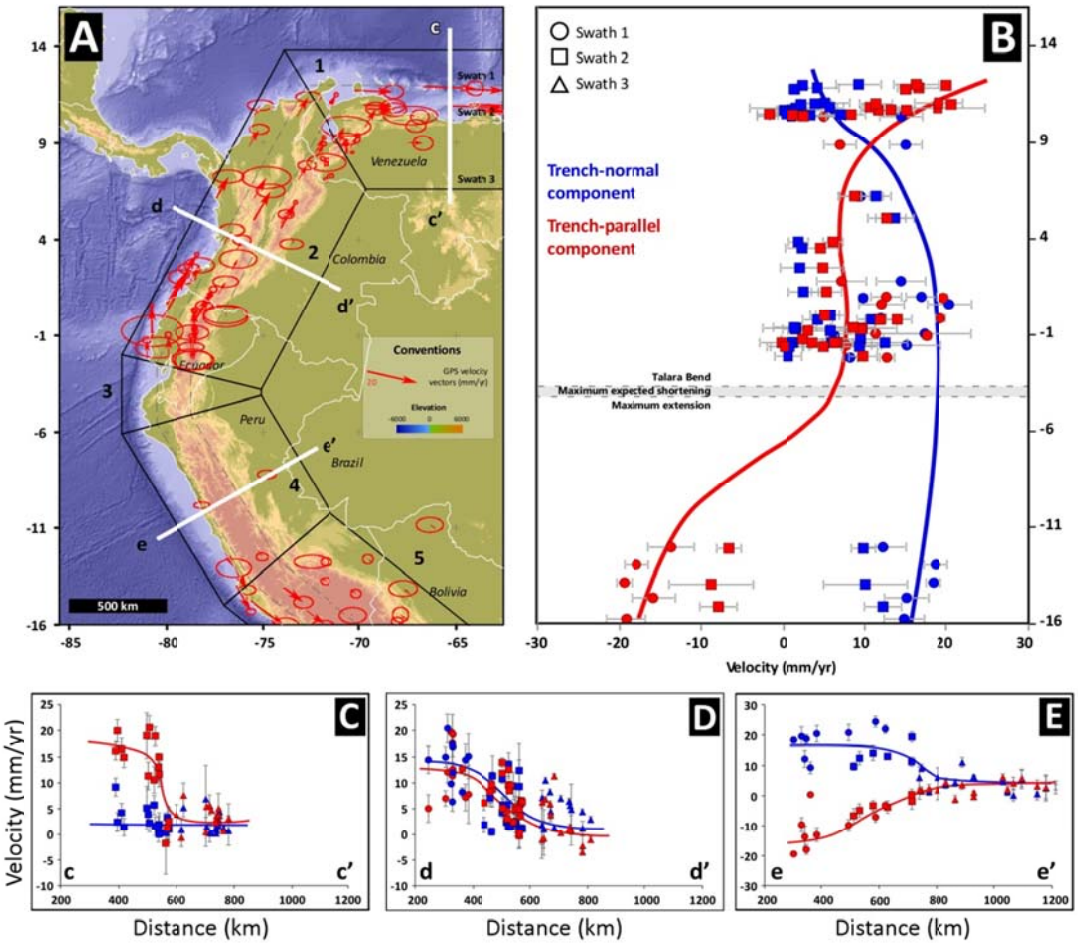
A
B
C
D
E
Swath 1
Swath 2
Swath 3
Trench-normal component
Trench-parallel component
Talara Bend
Maximum expected shortening
Maximum extension
Velocity (mm/yr)
Venezuela
Colombia
Ecuador
Peru
Brazil
Bolivia
Conventions
GPS velocity vectors (mm/yr)
Elevation
500 km
Velocity (mm/yr)
Distance (km)
Distance (km)
Distance (km)

**Figure 1.3 (a)** Trench-parallel component of GPS velocities. Swath profiles span the trench and 200 km inboard (Swath 1), from 200 to 400 km (Swath 2), and from 400 to 800 km (Swath 3) inboard. Numbers denote the different domains defined for the GPS analysis, 1: Venezuela, 2: Colombia, 3: Ecuador, 4 and 5 Peru. **(b)** Trench-parallel and normal components plotted as a function of latitude. Positive trench-parallel velocities are defined as counterclockwise. Note the opposing sense of motion in trench-parallel velocities around 5 S° at the TB. Red and blue lines are the approximate trends of trench parallel and normal components in the different domains. Components from Swath 3 are not shown for clarity. **(c)**, **(d)** and **(e)** are the trench normal and parallel projections of the velocity components for each domain. See Figure 3a for profile locations. CASM station from Kendrick et al., 2001 was excluded from the analysis.

**Figure 1.4**

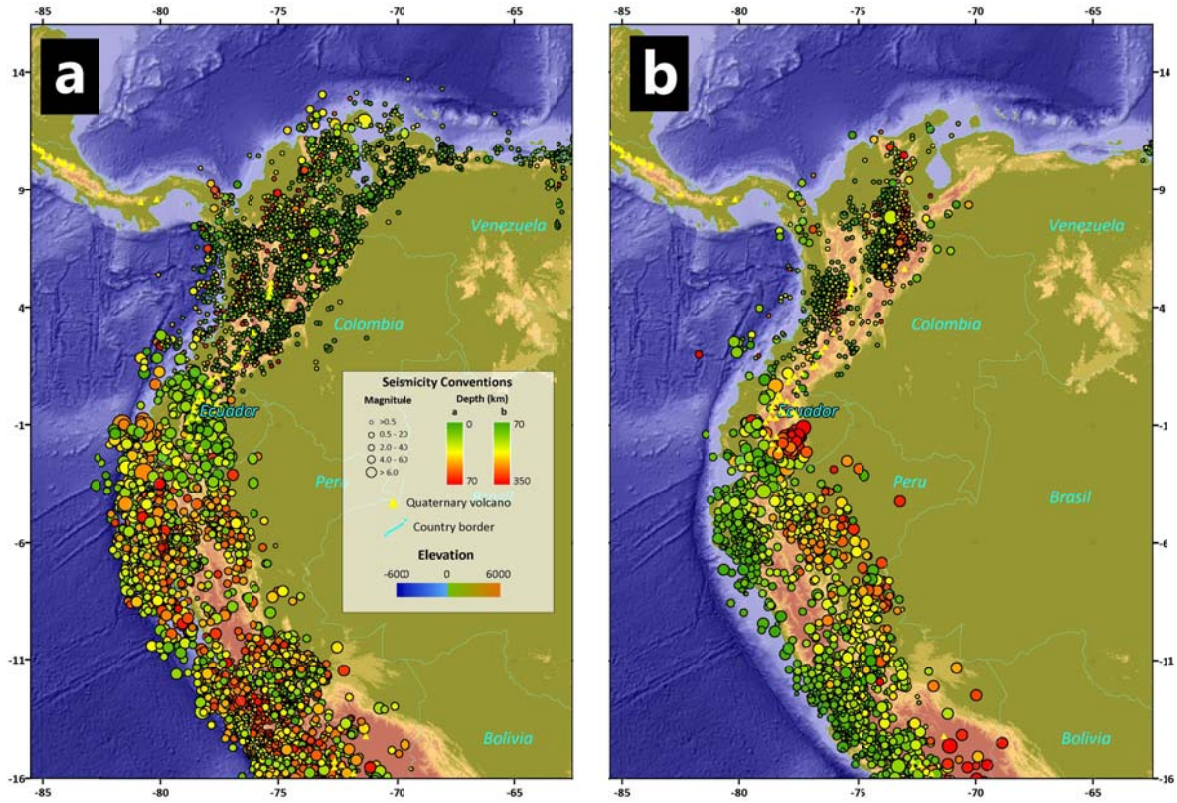
a
b
Venezuela
Colombia
Ecuador
Peru
Brasil
Bolivia
Seismicity Conventions
Magnitude
Depth (km)
a
b
0
70
70
350
Quaternary volcano
Country border
Elevation
-6000
0
6000

**Figure 1.4** Earthquake epicenters for the NW Andes from 1/1/2000-12/31/2010 from FUNVISIS (Venezuela), INGEOMINAS (Colombia), EPN (Ecuador) and IGP (Peru) catalogs (events < 0.4 RMS and Magnitude > 3.5). (a) Earthquake seismicity to 70 km depth. (b) Earthquake seismicity between 70 - 350 km depth.

# Active mountain building along the eastern Colombian Sub-Andes: A folding history from fluvial terraces across the Tame anticline, Llanos basin

**Gabriel Veloza**[1#]

**Michael Taylor**[1]

**Andrés Mora**[2]

[1]**Department of Geology**

**University of Kansas**

**Lawrence, KS 66045**

[2]**ICP-Ecopetrol**

**Bucaramanga, Colombia**

**#Email address: gvelozaf@ku.edu**

**To be submitted to GSA Bulletin**

## 2.1 ABSTRACT

Quaternary shortening and surface uplift is a prominent feature of the eastern foothills of the Eastern Cordillera of Colombia, where alluvial fan and fluvial deposits are folded and uplifted tens to hundreds of meters locally above basin base level. Here, we use detailed

geomorphic and structural analysis from a 300 $km^2$ seismic survey over the Tame anticline to investigate the relationship between finite shortening and surface uplift, its effects on landscape evolution, and trap initiation and development. A quantitative description of finite shortening of the pre-growth strata from line-length and excess area calculations along the fold trend are presented and then compared using the same approach as an added check on the uplift and shortening of geomorphic markers dated using in situ produced Terrestrial Cosmogenic Nuclides (TCN), providing the first estimates of Quaternary shortening along the Northern Colombian Andes at millennial time scales. The maximum finite shortening at the Tame anticline is 630±130 m at its southern end and decreases to the north to a maximum of 240±14 m. North-south variation in shortening is likely controlled by the geometry of inherited structures from Mesozoic extensional structures formed during the prior rifting phase. Our results reveal Quaternary shortening rates ranging from $1.3^{+0.2}_{-0.1}$ to $2.0^{+0.3}_{-0.2}$ mm/yr. These shortening rates are comparable to geodetic and longer term geologic estimates of shortening, suggesting that mountain building has been steady state along the eastern Andes of Colombia since the Late Miocene.

## 2.2 INTRODUCTION

The geometry of the Colombian Andes is largely controlled by the interaction between the Nazca, Caribbean and South American plates (Gutscher et al., 1999; Taboada et al., 2000; Cortés et al., 2005; Veloza et al., 2012). Late Cenozoic development of the Andes is thought to be controlled by reactivated Mesozoic rift structures and accretionary processes, forming the

Western, Central and Eastern cordilleras (Sarmiento, 2001; Mora et al., 2008). Such configuration makes the identification and quantification of the deformation transferred from the trench to the upper plate challenging in part because of the high number of seismically active structures present across Colombia (Dimaté et al., 2003; Veloza et al., 2012).

The northeastern foothills of Colombia (Figure 2.1) are a present day example for understanding the surface response of this three-plate interaction. This area has ample neotectonic structures recording deformation and transfer from the subduction zone plate boundary to more than 500 km inboard, as indicated by the high frequency – low magnitude seismicity, fault scarps, uplifted and warped fluvial terraces, and mapped active faults (Taboada et al., 2000; Dimaté et al., 2003; Veloza et al., 2012). Cenozoic shortening rates for this portion of the orogen are estimated to range between 1.8 and 5.0 mm/yr (Mora et al., 2010). Slightly slower shortening rates are observed today from the GPS surface velocity field (Trenkamp et al. 2002; Egbue and Kellogg, 2010), suggesting that convergence rates across the Eastern Cordillera have been significant since the Late Miocene. However, no millennial scale shortening rates have been determined for this portion of the Andes leading to a significant gap in knowledge between Miocene and recent time scales (e.g. Mora et al., 2010; Parra et al., 2009).

Quaternary shortening rates in contractional orogens with emergent faults are common in neotectonic and landscape evolution studies (e.g., Lavé and Avouac, 2000; Amos and Burbank, 2007) and is particularly valid for fault-bend folds or for fault-propagation folds, because these obey a well-known formulation that relates different parameters of the fold geometry to the slip on the fault plane (Suppe, 1983; Marshak & Mitra, 1988; Suppe and Medwedeff, 1990; Mitra, 1990; Hardy and Poblet, 2005). However, fault-tip folds or more generally, during the

initial stages of deformation, where folding and internal strain are the dominant mechanisms, the mechanics of fault-tip folding are less understood, as these structures do not obey specifics of the fault-related folding end member classification. These types of structures might evolve from detachment folding to progressive fault propagation (Mitra, 2002), creating symmetric or asymmetric structures (Suppe and Medwedeff, 1990; Mitra, 2002; Bernard et al., 2007; Daëron et al., 2007). Furthermore, the linkage between surface uplift and finite shortening in blind fault-related folds, recorded by pregrowth sequences, is not a trivial exercise and might shed light on understanding the development and kinematics of emergent folds, because preservation of geomorphic markers at the surface is usually poor due to erosion or non-deposition.

We implemented a simple formulation relating crestal uplift with cross sectional areas of the topography and present the first estimates of Quaternary surface uplift and shortening rates along the active thrust front in the retroarc of the northern Andes. Surface uplift and shortening rates are based on surface exposure ages of offset features using *in situ* produced terrestrial cosmogenic nuclides (TCN) and kinematic restoration of the Tame fold using a 3D seismic volume. Shortening calculated for the most frontal fault system of the Colombian Andes sheds light not only on the slip partitioning process as a consequence of the complex plate interaction in NW South America, but also helps to asses and mitigate seismic hazards in continental areas (England and Jackson, 2011) and to understand the dynamics of the petroleum system associated with the active basin.

## 2.3 SURFACE GEOLOGY OF THE TAME ANTICLINE

### 2.3.1 Basin Stratigraphy and Petroleum systems

The sedimentary sequence of the eastern foothills of the Eastern Cordillera and the Llanos basin is subdivided into three main sequences, deposited over Paleozoic sedimentary rocks and Proterozoic crystalline basement (Figure 2.1). Deposition started during the Upper Jurassic to Early Cretaceous with a c.a. 5 km thick sequence of conglomerates of the Buenavista Formation that change laterally to shales and salt beds, followed by the shale and mudstone-dominated Macanal, Caqueza and Fómeque formations (Mora et al., 2008). Middle to Late Cretaceous deposition is characterized by the Une, Chipaque and Guadalupe formations and is thought to represent proximal marine sequences associated with thermal subsidence phase of rifting (Sarmiento, 2001). The thickness of this postrift sequence reaches c.a. 2 km in the foothills area. Cessation of the post-rifting sequence is nearly coincident with the Cretaceous-Tertiary boundary and also represents a major change in sedimentary conditions shifting to sub-aerial deposits of the Barco, Cuervos and Mirador formations, which are less than 1 km in total thickness in the foothills area. These deposits record the easternmost influence of an emergent thrustbelt in the present location of the Central Cordillera (Bayona et al., 2008; Parra et al., 2009). This sedimentary sequence is capped by the Carbonera, León and Guayabo formations, which are thought to record development of the Eastern Cordillera thrust belt. This sequence of clastic sedimentary rocks reaches more than 3 km in thickness and records the eastward migration of the orogenic front with rates from 1.2 to 2.1 mm/yr over the last ~25 Ma (Parra et al., 2009).

The main source rock for Llanos basin petroleum accumulations is the mid-Cretaceous La Luna Formation and its lateral equivalents (Dzou et al., 1999; Elrich et al., 2000), which may

reach total organic content (TOC) of up to 6%. Almost all of the pre Late Miocene coarse-grained clastic intervals exhibit fair reservoir characteristics throughout the basin, and bear oil accumulations depending on the specific characteristics of the play system (Villamil, 2003; Toro et al., 2004). Trap generation is hypothesized to occur in two main pulses during peaks of thrust front advance, during Late Paleocene to Eocene, and during Late Miocene time. Oil generation and migration across the foothills depends on the local burial history, thermal maturation, and the geometry of structural traps. In general, the foreland basin receives a large proportion of hydrocarbons expelled from the Eastern Cordillera. One example is the large oil accumulations of the Cusiana Field in the eastern foothills that produce condensate oil and gas from the Guadalupe and Mirador formations (Cooper et al., 1995; Ramón and Fajardo, 2006), whereas the Rubiales Field, located in the distal foreland approximately 200 km from the easternmost thrust front, produces heavy oil from the Early Miocene Carbonera formation.

### 2.3.2 Structural setting of the Eastern Cordillera and Llanos Basin

The Eastern Cordillera of Colombia is a bivergent orogen resulting from E-W contraction structurally overprinting the preexisting Mesozoic extensional rift basins (Colleta et al., 1990; Dengo & Covey, 1993; Sarmiento, 2001; Mora et al., 2008). Two main families of structures are present in the orogen: (1) High angle basement involved reverse faults that may represent the inverted boundaries of Mesozoic rifts and (2) Thin skinned low-angle thrust faults, commonly detaching within the Mesozoic and Cenozoic sedimentary sequences (Kammer & Sanchez, 2006; Mora et al., 2008). Both structural families are common along the eastern side of the

orogen, whereas thin skin deformation is more dominant on the western flank of the Eastern Cordillera (Montes et al., 2005; Cortés et al., 2006; Sánchez et al., 2012).

Active faults in the sub-Andean zone of the Eastern Cordillera consist primarily of east-southeast directed thrust faults segmented along-strike by lateral ramps. Active deformation is indicated by high-frequency low-magnitude earthquakes recorded during the last ~20 years, including the 1995 devastating Mw=6.5 Tauramena event (Dimaté et al, 2003). Earthquake focal mechanisms indicate that the maximum principle stress ($\sigma_1$) direction is sub-horizontal and oriented WNW-ESE (Acosta et al., 2004; Cortés and Angelier, 2005), consistent with the geometry of seismically active thrust faults. In the northern part of the basin, the Cusiana - Yopal fault system represents the active and developing thrust front. The fault system is composed of fault segments tens of kilometers in length, that are predominantly east-directed thrusts, detaching from Cenozoic stratigraphic levels in the Samaricote syncline, that then connects along-strike northward into the Tame anticline via a relay ramp (Figure 2.2).

The Tame anticline, located in the northern Colombian sub-Andes, has a NNE trending fold axis and is growing above a blind fault system, associated with the easternmost thrust front of the Llanos basin. The anticline is ~16 km in the north-south direction and ~7 km wide east-west. Because of its antiformal geometry, the Tame anticline was targeted for oil exploration since the 1950's, resulting in the drilling of 4 wells and discovery of the Capachos field that produces approximately 1,000 barrels of oil per day (bopd) of 32° API oil. Although faulting is easily observed in subsurface seismic data, they are not readily observed at or near the surface, and the amount of displacement at depth is much larger than at the surface. Furthermore, surface

uplift is a response of folding and no emergent faults are observed, consistent with fault-propagation as the mechanism for fold growth of the Tame anticline.

### 2.3.3 Neotectonic development of the Tame Anticline

The warped and uplifted fluvial terraces in the study area were mapped using a 30m digital elevation model (DEM) produced from the Shuttle Radar Topography Mission (SRTM) that was augmented by our field observations. The terraces were classified according to their relative elevation to other sub-horizontal terrace surfaces and their geomorphic characteristics (Figure 2.2). For example, the youngest elevated deposits (T5) are characterized by a low degree of weathering (i.e., surface modification), in contrast to older terrace levels (T1), where locally incision is more pronounced on the eastern side of the fold. The terrace elevation was measured in the field and compared to the altitude of the SRTM DEM that has a normally distributed 1σ uncertainty of 4 m for elevation (Rabus et al., 2003).

Drainage patterns vary along-trend of the Tame anticline. In the northern and southern ends of the fold, where the highest relief is observed, the drainage is deflected around the nose of the growing fold. The central portion of the fold where the local relief is lower, the drainage is focused along the antecedent Macaguana creek (Figure 2.2). Drainage areas along the fold are in general small, and sourced within the eastern foothills, which might represent small discharge and low stream power (Dietrich et al., 1992). This suggests that the location of the antecedent Macaguana creek is structurally controlled and that incision is not purely incidental or controlled by erosive effects of stream power, as observed in other active thrustbelts (Medwedeff, 1992; Burbank et al., 1996; Lave and Avouac, 2000). The development of

topography and the deflected drainage patterns suggests that locally, uplift rates should outpace deposition or erosion.

The uplift of the terraces is interpreted to be a response of slip on the blind Cusiana-Yopal fault system. We estimated the amount of uplift by using topographic profiles along the folded terraces and comparing them to the elevations of the Llanos basin base level that slopes eastward by around 1°. These elevations are projected onto the same profile, so both elevations are collocated at the same position with respect to the aggradation–base level of the Llanos basin (Figure 3a). Uplift varies between 0 and ~200 m for the most elevated terrace surface (T1), which is west tilted up to 6.9°, T3 has a surface tilt of 4.7° west, and the youngest terrace, T4 is subhorizontal with a minor tilt of about 0.3° west. This incremental tilting and warping of the terrace surfaces reflects the progressive limb growth and slip of the blind structure.

### 2.3.4 Terrace Geochronology

*In situ* Terrestrial Cosmogenic Nuclides (TCN) uses the concentration of the $^{10}$Be isotope created during the spallation of oxygen in the quartz structure, arising from the high-energy collision of cosmic particles bombarding Earth's surface. The concentration of $^{10}$Be is thus proportional to the duration time of exposure at the Earth's surface for the sediments. A sample's $^{10}$Be concentration depends on the production rate of $^{10}$Be, which is a function of the cosmic ray flux onto Earth's surface and is affected by the samples position (i.e., latitude and altitude), and the amount of time that the grains have experienced exposure to cosmic rays during prior transport to its final depositional setting. The $^{10}$Be concentration is used to

estimate the age since the deposits have been abandoned by the river system or uplifted relative to the river bed or base level of the basin (Gosse and Philips, 2001). The concentration of TCN isotopes also varies with depth below the surface, since high-energy particles are attenuated with increasing depth. Depth profiling is a useful technique in that it allows for a more robust estimation of the surface abandonment age by using the variation of $^{10}$Be with depth, with the asymptote of the concentration curve indicating the inherited value (Granger and Riebe, 2007; Hidy et al., 2010).

The following criteria for selecting the sampled terraces are as follows: (1) We avoid surfaces showing signs of significant incision and surficial modification due to land sliding or anthropogenic processes, (2) Laterally continuous surfaces are ideal as they suggest less erosion. (3) Samples were collected at least 20 m away from the terrace edges (Figure 2.2). Between 4 and 6, 2 kg bag of quartz rich sand samples were collected at different depths below the upper mixing zones in 2 m deep hand-dug pits along a 5 cm thick horizontal interval. Soil horizons and mixing zones typically extend down to 0.6 m below the surface in tropical settings.

Sample preparation was conducted at PRIME Laboratories at Purdue University, following the procedures and standards suggested by Gosse and Phillips (2001). Accelerator Mass Spectrometry (AMS) measurements were also conducted at PRIME, which reports 5% error (1σ) on its measurements (Table 2.1). Surface exposure ages were calculated using the Hidy et al., (2010) v. 1.2 Matlab code with 100,000 iterations for concentration versus depth profile solutions within the 2σ error level, encompassing measurement precision, surface production rates, density, and erosion threshold uncertainties. Age calculations take into account primary (spallation) and secondary (thermal, epithermal neutron capture, and muonic) nuclide

production (Gosse and Philips, 2001; Hidy et al., 2010). Site production rates were calculated using the Cronus online calculator (Balco et al., 2008), and using a 10% variability as 1σ error on the calculation, which includes variation depending on the chosen scaling scheme for production rates.

Since the model ages for individual depth profiles did not converge to a single solution, we view the modal ages as the most appropriate representation for the age of abandonment for these surfaces (Figure 2.4). The surface exposure ages for the three sampled terraces are T1: $89.6^{+17.5}_{-11.1}$, T3: $48.2^{+5.6}_{-7.2}$, and T4: $33.1^{+5.0}_{-5.5}$ ka. Although we avoided incised and eroded surfaces in the field, we assume a maximum erosion threshold of 1 m for all surfaces. This erosion threshold does not have a significant impact on our age estimations within the 1σ calculation. The calculated ages are consistent with the elevation differences between the sampled terraces and the Llanos basin base level. The oldest terrace is located at the highest elevations and the youngest age corresponds to the lowermost sampled level. Summaries for surface exposure ages for each terrace are provided in Table 2.2.

### 2.3.5 Uplift Rates

The elevations of the sampled fluvial terraces range between 450 and 580 meters above mean sea level - the Llanos basin base level ranges from 420 m at the western side of the fold to 270 m near the eastern flank, with the bajada surface dipping ~1° towards the east (Figures 2 and 3). The uplift of the dated terraces, calculated as the difference between the terrace elevation and the high order polynomial interpolation of the Llanos basin base level, varies between 116 and 177 meters (Figures 3 and 5). The antecedent Macaguana creek elevation was

not used to obtain terrace uplift because it is at a higher elevation than the interpolated base level of the basin, consistent with the idea that it is currently unable to keep pace with uplift and will likely become a wind gap.

Sampled sites in T3 and T4 are located at the maximum terrace elevations, and thus are recorders for maximum uplift. However, the location of the sampled site in the T1 terrace is not at the site of maximum uplift, but we assume that locally, the terrace tread was abandoned at the same time (Figure 2.3). Therefore, based on the chronological control of the geomorphic surfaces, and assuming a maximum uplift from the largest difference between the terraces and the local base level, which we assume has a uniformly distributed 1σ uncertainty of 15 m, the Monte Carlo simulation after 100,000 iterations for surface uplift rates are T1: $2.3^{+0.2}_{-0.2}$ mm/yr, T3: $3.1^{+0.4}_{-0.3}$ mm/yr and T4: $3.5^{+0.5}_{-0.4}$ mm/yr (Figure 2.5). In the following we investigate the long term geologic shortening rates across the Tame anticline using seismic reflection data, followed by a comparison with the neotectonic shortening rates.

## 2.4 SUBSURFACE GEOLOGY OF THE TAME ANTICLINE

The 3D seismic survey over the Tame anticline was acquired in 2002, covering approximately 300 km$^2$. Bin size parameters are 30x60 m with a sample rate of 4 ms. Interval velocities and velocity surveys from one of the wells within the anticline is used for seismic depth conversion using approaches widely used for the Llanos basin (Chermak et al., 2007), although we assume no local lateral variations in velocity for the Tame anticline. Nine key horizons were mapped and well-tied to biostratigraphic information from surrounding wells (Jaramillo et al., 2011). Over one hundred seismic sections were interpreted to constrain the

detailed fold geometry, which then were gridded using a convergent interpolation algorithm to create a structural contour map for each interpreted horizon (Figure 2.6). From the hundred interpreted sections, thirty eight structural cross sections, evenly spaced every 600 meters along the fold trend were selected to perform geometric and kinematic restorations to determine the shortening magnitude using different approaches, which are discussed in more detail in Section 3.1.

Basement structures are an important control on both Cretaceous deposition and sedimentation patterns and Neogene deformation, as observed in the seismic data and interpretation (Figures 7 and 8). The thickness difference between the hanging wall and the footwall of the Mesozoic west dipping normal fault is approximately 1.5 km (Figure 2.7), where the fault was likely active after deposition of the K1 horizon. The west side of the basement high was originally bounded by a west-dipping normal fault, whereas the eastern side is gently east dipping. The northern and southern sides of the basement high are interpreted to be fault bounded, but we cannot discern the details of the kinematic history – Assuming they moved during the development of the north-south striking dip slip structures, they were either left lateral strike slip faults, or north and south dipping normal faults, that were later reactivated as right lateral faults based on separations observed in the seismic data (Figure 2.8). Although the reactivated right-lateral faults do not cut and offset the entire sequence and tip out at ~5 km depth, they affect the entire sequence by localizing the terminations of the anticline and the drainage patterns above them (Figures 1 and 6).

Along-trend changes in fault geometry and structural style are seemingly controlled by basement heterogeneities and the modern strain field, which is oriented WNW-ESE

(Colmenares and Zoback, 2003; Cortés and Angelier, 2005). In the southern portion of the Tame anticline, fault slip is focused on a single east-directed thrust fault, whereas in the northern segment, deformation is expressed as several east-directed fault splays bounded by a west directed passive roof thrust linking with the lowermost frontal fault. The fault geometry is consistent with the fold vergence, which changes from slightly west vergent in the north to strongly east vergent in the south (Figures 6 and 7).

### 2.4.1 Finite shortening

Models commonly used to constrain the structural evolution, shortening, and surface uplift of fault-related folds rely primarily on their limbs and associated fault geometry (Suppe, 1983; Suppe and Medwedeff, 1990; Avouac et al., 1993). However, fault-tip folds commonly do not bear simple structural relationships between the parameters controlling their fold evolution, and depend largely on their mechanical stratigraphy (Mitra, 2002). In an attempt to resolve the complexities between the aforementioned structural parameters, different methodologies for describing fold evolution, including growth strata and surface uplift have recently been developed (Hardy and Poblet, 20005; Bernard et al., 2007; Daëron et al., 2007; Gonzalez Mieres & Suppe, 2012).

However, in the Tame anticline, the shallower portion of the available seismic information does not have the necessary resolution to resolve the geometry of growth strata making a detailed folding history difficult. Therefore, we use a simple approach similar to the excess area method (Epard and Groshong, 1993; Gonzalez-Mieres and Suppe, 2012; Wiltschko and Groshong, 2012) to quantify the long-term shortening recorded by the dated geomorphic

markers above the Tame anticline, using finite shortening measured from the pre-growth sequence.

Fault-tip structures are characterized by shortening accumulated by folding and internal strain. This basic assumption has led to the main formulation relating excess area of any particular horizon within the deformed sequence to the amount of shortening undergone by that particular horizon, which is related to the depth to detachment, by the following relationship:

$$Hd = \frac{Asr}{Sl} (1)$$

Where $Sl$ is the line-length shortening, that is the difference between the length of the deformed bed ($Ld$) and the length of the cross sectional area ($L$), $A$ is the excess area and $Hd$ is the depth to the detachment (Chamberlin, 1910) (Figure 2.9). However, this formulation has been recently revised based on the uncertainties associated with overestimating the depth to detachment (Mitra, 2002; Wiltschko and Groshong, 2012). Mitra (2002) suggests that overestimating the depth to detachment from Chamberlin's (1910) equation arises from not taking into account areas below the regional level. However, these areas commonly represent only a small fraction of shortening. On the other hand, Epard and Groshong (1993), suggests that the disparity in the original Chamberlin formulation arises from not taking into account internal strain (i.e., homogeneous strain). Epard and Groshong, (1993), thus propose that finite shortening (*St*) of a cross sectional area is the derivative of the excess area over an arbitrary reference level, that then estimates the depth to the detachment and also determines if mass flows into the core of the anticline, where:

$$St = \frac{\delta A}{\delta Hd} \ (2)$$

We note that internal strain (ε) is below the resolution of seismic data, but structures commonly observed at the outcrop and hand sample scales suggest this approach is valid (Wiltschko and Groshong, 2012). Then, line-length shortening ($Sl$) used in (1) represents only a portion of the finite shortening ($St$), and the difference between these two is the internal strain (ε) for the cross sectional area, that can be calculated from:

$$\varepsilon = St - Sl \ (3)$$

However, internal strain ($e$) itself may not be particularly useful, because it depends on the shortening values for each cross sectional area. So, the internal strain (ε) can be rewritten as:

$$\varepsilon = Sl/St \ (4)$$

Where the ratio of line-length and finite shortening describes the proportion of finite deformation related to internal strain. Using the same basic assumptions, $St$ is can be also translated to the thickness domain, which under certain circumstances may lead to more precise estimates of total shortening (Gonzalez-Mieres and Suppe, 2006).

Using a combination of approaches from Epard and Groshong (1993) and Gonzalez-Mieres and Suppe (2006) we determine the total shortening of the sequence and also derive the contribution of internal strain (ε) for the Tame anticline since the initiation of folding, and also quantify variations along the fold trend (Figure 2.10). We also solve for the depth to the detachment as a blind test for the interpretation (Figure 2.10) used to estimate the shortening of the deformed geomorphic markers. Longitudinal swath topographic profiles over the Tame anticline, line-length and area of excess shortening values and depth to detachment using balanced cross-sections are presented using along-trend projections, allowing for a direct

comparison between finite shortening and uplift values (Figure 2.10). For consistency, we discuss variations in fold kinematics beginning from the south.

Along-trend, the maximum line-length ($Sl$) and finite ($St$) shortening are observed in the segment between kilometers 3 and 10 from the southern end of the fold, reaching a maximum finite shortening ($St$) of 630±130 m at kilometer 8 (Figure 2.10). In contrast, at the northern end of the fold, between kilometers 14 and 20 shows less shortening, with finite shortening ($St$) of 220±20 m at kilometer 17.5. The large uncertainty in fold metrics, between kilometers 11 and 14 is consistent with the structural saddle implying less shortening, leading to a lower $r^2$ values and associated errors in the calculations. The saddle location appears to be structurally controlled because it is a consistent structural feature throughout the pre-growth sequence (Figure 2.7). In this case the line-length ($Sl$) shortening exhibits smaller uncertainties. For example, at kilometer 14 the line-length shortening ($Sl$) is 110±10 m, compared to 94±181 m of calculated finite shortening ($St$). Thus, in areas of small shortening line-length methods might be a more reliable tool to estimate shortening.

In general line-length shortening ($Sl$) represents about 35% of the finite shortening ($St$). The ratio of $Sl/St$, plotted for each interpreted section on Figure 10 indicates that a considerable portion of the fold growth is dominated by internal deformation. The vertically homogeneous line-length shortening indicates that there is negligible layer-parallel simple shear. Observed areas of excess, between 0.2 and 1.6 $km^2$ might represent flow of material into the core of the anticline from adjacent areas (Wiltschko and Chapple, 1977), as commonly observed in other fold-dominated structures in the Appalachians (Wiltschko and Chapple, 1977) or in the Niger delta (Gonzalez-Mieres and Suppe, 2006). This scenario seems likely since salt and gypsum

deposits are commonly observed in other fault-related folds along the Eastern Cordillera foothills and hinterland (Mora et al., 2008).

The depth to detachment ($Hd$) for the thirty eight balanced cross-sections is consistent at approximately 8 km (Figure 2.10). Slight differences may be due to small errors in the construction of the sections or to lateral variations in seismic velocity. This depth is consistent with the major rheological interface of the area, which is the unconformity between the sedimentary cover and the crystalline basement, where a detachment surface will most likely develop. Although the detachment surface is not clearly observed in the seismic information, the basement is, and the faults cutting upward and across the pre-growth sequence sole into this major interface (Figure 2.7).

Surface uplift is in agreement with the shortening calculations (Figure 2.10). Maximum surface elevations are observed in the south between kilometers 4 to 8, reaching a maximum of ~600 mamsl. Between kilometers 8 -12 the location of the saddle is clearly observed in Figure 10, with maximum elevations of ~420 mamsl. The northward decrease in shortening is reflected in the topography, where the surface reaches a maximum of ~500 mamsl at kilometer 13.

Although natural folds commonly do not prescribe to any end-member model of fold evolution, the nearly constant crestal uplift of each interpreted horizon, consistent with minimal layer-parallel simple shear, and the nearly constant decrease of fold amplitude with increasing depth (Figure 10 and 6) lead us to suggest that the Tame anticline is a self-similar, box-like fault-tip fold. The calculated depth to detachment (Figure 2.10) agrees with the observed depth of the basement hanging wall of the normal fault. Thus, this relationship

reinforces our initial hypothesis that the primary structural control for fold development is the prior structural configuration of the basement.

### 2.4.2 Quaternary shortening

Poor seismic imaging of the uppermost first second (TWT) of seismic data prevents us from resolving growth strata at the near surface. Additionally, the finite shortening of the uppermost stratigraphic horizon (G1 in Figure 7) is equal within error to the shortening of the deeper horizons, representing minimal layer-parallel shear. Based on these, we also assume that fold growth should have started at least after the deposition of the G1 horizon, which was deposited approximately at 2 Ma (Figure 2.7). Using the same approach for the finite shortening calculations, we calculate shortening for the uplifted and warped fluvial terraces to determine Quaternary shortening rates.

Using the topographic profiles (Figure 2.3) we reconstructed the pre-deformation and pre-erosion terrace geometry to agree with the regional base level of the Llanos basin, following as well the overall fold geometry, recorded in different geomorphic markers and in the pre-growth sequence (Figure 2.11). We assume a 1σ uplift uncertainty of 15 meters for the elevations that we propagate into the excess area calculations. Using the depth to detachment determination, we calculate a Quaternary shortening rate $Sq$ for terrace levels T1: $1.3^{+0.2}_{-0.1}$, T3: $2.0^{+0.3}_{-0.2}$ and T4: $2.0^{+0.3}_{-0.2}$ mm/yr.

## 2.5 DISCUSSION

Surface uplift can occur when tectonic uplift exceeds sedimentation and erosion rates (Burbank et al., 1996). Although we do not have any estimate for erosion nor deposition rates, we do know that the uplift rate has outpaced these two, not only where the greatest uplift is observed in the south but also in the north, because the drainages are deflected in both areas. Therefore, taking into account the small drainage area of the antecedent Macaguana creek as an indication for stream power erosion (Dietrich et al., 1992), the location of the saddle observed throughout the entire stratigraphic sequence (Figures 6 and 7), and the small amount of shortening for this portion of the fold (Figure 2.10), suggests that its location is not coincidental. The location of the saddle appears to be structurally controlled and may represent the location of a relay structure between the fold-bounding faults on the north and south sides of the Tame anticline.

To explain the decrease in total shortening along-trend, we suggest that the east-striking lateral ramps bounding the Tame anticline and observed in the seismic data are acting as barriers for fold propagation to the north and south. This may be the case for the Tame anticline, and may be a common structure associated with growing folds in the Llanos basin such as the Samaricote syncline and the Corozal anticline, which are also bounded by lateral ramps (Figure 2.1), as well as other active thrust belts (Scharer et al., 2004; Chen et al., 2007).

Our Quaternary shortening rates for the Tame anticline are in agreement with geodetic shortening rates for this portion of the Colombian and Venezuelan sub-Andes. Horizontal velocities near in the Colombian foothills, south of the study area is approximately 2.3 mm/yr (Trenkamp et al., 2002), and in Venezuela, north of the Tame anticline is 3.1 mm/yr (Pérez et al., 2011), suggesting that active faults bounding the Llanos basin should be incorporated into

any seismic hazards assessment for the Colombia interior. Understanding seismic hazards and strain accumulation in the continental interiors is an important step in risk mitigation, especially in developing countries (England and Jackson, 2011). For the Llanos region, the largely populated cities as Yopal and Villavicencio are especially prone to seismic hazards as they are located above the Cusiana-Yopal fault system.

Along-trend variations in fold geometry are commonly observed along the Eastern Cordillera and Upper Magdalena Valley basins (Cortés et al., 2005). Two main hypotheses have been proposed to explain these variations – The first suggests plate reorganizations can produce changes in the strain field, which is based on kinematic indicators observed in syn and post-rift sequences, consistent with at least two deformation phases for the Eastern Cordillera (Cortés and Angelier, 2005). These observations document a change from SW-NE to NW-SE in the $e_1$ orientation from the Early Cretaceous to the Early Miocene, respectively. The second hypothesis is related to the response of the sedimentary cover to deformation over pre-existing basement configurations during structural inversion, and slip partitioning because of the regional plate configuration and convergence obliquity (Veloza et al., 2012).

The active basinward propagation of the thrust front of the Colombian sub-Andes indicates the thrust wedge was supercritical between 2 Ma and 0.5 Ma ago. Furthermore, long term shortening rates for this portion of the Andes (Parra et al., 2009; Mora et al., 2010) attest that the basinward advance occurred at similar order of magnitude rates, in the range of 2-10 mm/yr. This relationship is further supported by the lack of observations for Quaternary internal shortening or active thrust faults in the local hinterland. Further mapping will be a true test of this relationship.

The implications for oil exploration and play assessment in the Llanos basin are beyond the scope of this work. However, our results are contrary to the main belief that oil generation and migration occurred during peak mountain building events, during the middle Cenozoic (Toro et al., 2004) and Miocene (Villamil et al., 2003). Rather, our findings show that oil migration is a continuous process in the structurally deeper areas of the Eastern Cordillera, once the prime temperature and burial conditions are attained by the source rocks. For example, in the lower structural levels west of the Tame anticline, the La Luna formation is the main source rock for the Llanos basin (Dzou et al., 1999; Ramón and Dzou, 2001) at approximately 4 km depth, within the oil generation window. Recent migration has charged active and youthful structures, such as the Tame anticline. However the limiting factor for the development of such young plays is economic, because the volume of hydrocarbons expelled and stored since trap formation is small. Additionally, it should be noted that seismically active faults are located adjacent to the largest producing onshore petroleum reserves in Colombia (e.g. Cusiana Field), which is a significant component of the Colombian economy.

## 2.6 CONCLUSIONS

Quaternary surface uplift and shortening for the Tame anticline is investigated in the Colombian sub-Andes by detailed structural analysis and geochronological control of offset geomorphic markers. Our data and interpretation of the folding history can be summarized in the following conclusions:

(1) The Tame anticline is a prime example of an actively advancing thrustbelt, represented by slip on the Cusiana-Yopal fault system in the Colombian sub-Andes. Shortening

estimates calculated from the cross sectional areas from the 3D seismic volume show that finite shortening decreases northward, from a maximum of 630±130 m in the southern end of the fold to a maximum in the northern end with 240±14 m. The combination of geomorphology, seismic reflection data, and cross section reconstruction for the Tame anticline illustrates well the relationship between fold development and lateral ramps, which can act as structural barriers to propagating fault related folds.

(2) *In situ* Terrestrial Cosmogenic Nuclide dating has proven to be useful approach to determine surface abandonment ages of geomorphic markers in actively tectonic areas, even in the tropical latitudes of the Colombian sub-Andes. The surface abandonment ages for the incised and folded terraces are: T1: $89.6^{+17.5}_{-11.1}$, T3: $48.2^{+5.6}_{-7.2}$, T4: $33.1^{+5.0}_{-5.5}$ ka. The magnitude of incision for the geomorphic markers varies between 116 and 177 meters above the local base level of the Llanos Basin.

(3) Surface uplift rates across the Tame anticline is between $2.2^{+0.2}_{-0.2}$ and $3.5^{+0.5}_{-0.6}$ mm/yr. The excess area methodology provides a quantitative approach to determine not only finite shortening in a well constrained sub-surface seismic image of a fold, but also modern shortening based on the topography of the emergent structure. The Quaternary horizontal shortening rate is calculated to range from $1.3^{+0.2}_{-0.1}$ to $2.0^{+0.3}_{-0.2}$ mm/yr.

(4) Using the calculated Quaternary shortening rates, fold initiation is constrained to be approximately 0.4 Ma, where folding and internal strain are the dominant deformation mechanisms for active fault-tip folding. Variations along fold trend in deformation style

are mechanically controlled by the buttressing effect imposed by inherited basement heterogeneities from prior rift related deformation.

(5) Although not directly addressed in this study, an implication is that the Colombian sub-Andes are a natural laboratory to investigate the kinematics of thrust belt development and to understand how strain is transmitted from the plate boundary subduction zone to the retroarc regions. This relationship has profound implications for earthquake hazards assessment, the structural and dynamic controls on the distribution of petroleum resources, and in general how orogenic systems evolve at different time scales.

**ACKNOWLEDGEMENTS**

We thank Ecopetrol-ICP and KU for funding through the project "Cronología de la deformación en las cuencas Subandinas". Discussion with Antonio Teixell, Ken McClay, Richard Styron, Andrew McCallister and Maureen Logan greatly improved our thoughts on the evolution and kinematics of the Tame anticline. We are also indebted to Marc Caffee, Thomas Clifton, and Greg Chmiel for training and support during the laboratory phase of the project at PRIME laboratory at Purdue University. Seismic interpretation and depth conversion were performed in Move™ (Midland Valley Exploration) software grant to M. Taylor. Seismic information was provided by Ecopetrol S.A., acquired under the Capachos Association Contract with Repsol.

**REFERENCES**

- Acosta, J., Lonergan, L., and Coward, M., 2004, Oblique transpression in the western thrust front of the Colombian Eastern Cordillera: Journal of South American Earth Sciences, v. 17, no. 3, p. 181-194.
- Amos, C. B., Burbank, D. W., Nobes, D. C., and Read, S. A. L., 2007, Geomorphic constraints on listric thrust faulting: Implications for active deformation in the Mackenzie Basin, South Island, New Zealand: J. geophys. Res, v. 112, no. B03S11, p. B03S11.
- Avouac, J. P., Tapponnier, P., Bai, M., You, H., and Wang, G., 1993, Active thrusting and folding along the northern Tien Shan and late Cenozoic rotation of the Tarim relative to Dzungaria and Kazakhstan: Journal of Geophysical Research, v. 98, no. B4, p. 6755-6804.
- Balco, G., Stone, J. O., Lifton, N. A., and Dunai, T. J., 2008, A complete and easily accessible means of calculating surface exposure ages or erosion rates from< sup> 10</sup> Be and< sup> 26</sup> Al measurements: Quaternary Geochronology, v. 3, no. 3, p. 174-195.
- Bayona, G., Cortés, M., Jaramillo, C., Ojeda, G., Aristizabal, J. J., and Reyes-Harker, A., 2008, An integrated analysis of an orogen–sedimentary basin pair: Latest Cretaceous–Cenozoic evolution of the linked Eastern Cordillera orogen and the Llanos foreland basin of Colombia: Geological Society of America Bulletin, v. 120, no. 9-10, p. 1171-1197.
- Bernard, S., Avouac, J. P., Dominguez, S., and Simoes, M., 2007, Kinematics of fault-related folding derived from a sandbox experiment: J. geophys. Res, v. 112, p. B03S12.
- Burbank, D., Meigs, A., and Brozović, N., 1996, Interactions of growing folds and coeval depositional systems: Basin Research, v. 8, no. 3, p. 199-223.

- Chamberlin, R. T., 1910, The Appalachian folds of central Pennsylvania: The Journal of Geology, v. 18, no. 3, p. 228-251.
- Chen, J., Heermance, R., Burbank, D. W., Scharer, K. M., Miao, J., and Wang, C., 2007, Quantification of growth and lateral propagation of the Kashi anticline, southwest Chinese Tian Shan: J. geophys. Res, v. 112, p. B03S16.
- Chermak, A., Veloza-Fajardo, G., and Ramon, J. C., 2009, Depth Conversion in the Llanos Basin: Workflow to reduce fault shadow effect., X Simposio Bolivariano de Cuencas Subandinas, Volume 1.
- Colletta, B., Hebrard, F., Letouzey, J., Werner, P., and Rudkiewicz, J., 1990, Tectonic style and crustal structure of the Eastern Cordillera (Colombia) from a balanced cross-section: Petroleum and tectonics in mobile belts: Paris, Editions Technip, p. 81-100.
- Colmenares, L., and Zoback, M. D., 2003, Stress field and seismotectonics of northern South America: Geology, v. 31, no. 8, p. 721-724.
- Cooper, M., Addison, F., Alvarez, R., Coral, M., Graham, R., Hayward, A., Howe, S., Martinez, J., Naar, J., and Peñas, R., 1995, Basin development and tectonic history of the Llanos Basin, Eastern Cordillera, and middle Magdalena Valley, Colombia: AAPG Bulletin-American Association of Petroleum Geologists, v. 79, no. 10, p. 1421-1443.
- Cortés, M., and Angelier, J., 2005, Current states of stress in the northern Andes as indicated by focal mechanisms of earthquakes: Tectonophysics, v. 403, no. 1, p. 29-58.
- Cortés, M., Angelier, J., and Colletta, B., 2005, Paleostress evolution of the northern Andes (Eastern Cordillera of Colombia): Implications on plate kinematics of the South Caribbean region: Tectonics, v. 24, no. 1.

- Cortés, M., Colletta, B., and Angelier, J., 2006, Structure and tectonics of the central segment of the Eastern Cordillera of Colombia: Journal of South American Earth Sciences, v. 21, no. 4, p. 437-465.
- Daëron, M., Avouac, J. P., Charreau, J., and Dominguez, S., 2007, Modeling the shortening history of a fault tip fold using structural and geomorphic records of deformation: J. geophys. Res, v. 112, p. B03S13.
- Dengo, C. A., and Covey, M. C., 1993, Structure of the Eastern Cordillera of Colombia: implications for trap styles and regional tectonics: AAPG BULLETIN, v. 77, p. 1315-1315.
- Dietrich, W. E., Wilson, C. J., Montgomery, D. R., McKean, J., and Bauer, R., 1992, Erosion thresholds and land surface morphology: Geology, v. 20, no. 8, p. 675-679.
- Dimate, C., Rivera, L., Taboada, A., Delouis, B., Osorio, A., Jimenez, E., Fuenzalida, A., Cisternas, A., and Gomez, I., 2003, The 19 January 1995 Tauramena (Colombia) earthquake: geometry and stress regime: Tectonophysics, v. 363, no. 3-4, p. 159-180.
- Dzou, L. I., Holba, A. G., Ramón, J. C., Moldowan, J. M., and Zinniker, D., 1999, Application of new diterpane biomarkers to source, biodegradation and mixing effects on Central Llanos Basin oils, Colombia: Organic geochemistry, v. 30, no. 7, p. 515-534.
- Egbue, O., and Kellogg, J., 2010, Pleistocene to Present North Andean “escape”: Tectonophysics, v. 489, no. 1, p. 248-257.
- England, P., and Jackson, J., 2011, Uncharted seismic risk: Nature Geoscience, v. 4, no. 6, p. 348-349.
- Epard, J. L., and Groshong, R. H., 1993, Excess area and depth to detachment: AAPG BULLETIN, v. 77, p. 1291-1291.

- Erlich, R., Macsotay I, O., Nederbragt, A., and Antonieta Lorente, M., 2000, Birth and death of the Late Cretaceous: Journal of South American Earth Sciences, v. 13, no. 1-2, p. 21-45.
- Frankel, K., Finkel, R., and Owen, L., 2010, Terrestrial cosmogenic nuclide geochronology data reporting standards needed: Eos Trans. AGU, v. 91, no. 4.
- Gonzalez-Mieres, R., and Suppe, J., 2006, Relief and shortening in detachment folds: Journal of Structural Geology, v. 28, no. 10, p. 1785-1807.
- -, 2012, Shortening histories in active detachment fold based on area-of-relief methods, in McClay, K., Shaw, J., and Suppe, J., eds., Thrust Fault-Related Folding, Volume 94: AAPG Memoir.
- Gosse, J. C., and Phillips, F. M., 2001, Terrestrial in situ cosmogenic nuclides: theory and application: Quaternary Science Reviews, v. 20, no. 14, p. 1475-1560.
- Granger, D., and Riebe, C., 2007, Cosmogenic nuclides in weathering and erosion: Treatise on Geochemistry: Oxford, Pergamon, p. 1-42.
- Gutscher, M. A., Malavieille, J., Lallemand, S., and Collot, J. Y., 1999, Tectonic segmentation of the North Andean margin: impact of the Carnegie Ridge collision: Earth and Planetary Science Letters, v. 168, no. 3, p. 255-270.
- Hardy, S., and Poblet, J., 2005, A method for relating fault geometry, slip rate and uplift data above fault-propagation folds: Basin Research, v. 17, no. 3, p. 417-424.
- Hidy, A. J., Gosse, J. C., Pederson, J. L., Mattern, J. P., and Finkel, R. C., 2010, A geologically constrained Monte Carlo approach to modeling exposure ages from profiles

of cosmogenic nuclides: An example from Lees Ferry, Arizona: Geochemistry, Geophysics, Geosystems, v. 11, p. Q0AA10.

- Jaramillo, C. A., Rueda, M., and Torres, V., 2011, A palynological zonation for the Cenozoic of the Llanos and Llanos Foothills of Colombia: Palynology, v. 35, no. 1, p. 46-84.
- Kammer, A., and Sánchez, J., 2006, Early Jurassic rift structures associated with the Soapaga and Boyacá faults of the Eastern Cordillera, Colombia: Sedimentological inferences and regional implications: Journal of South American Earth Sciences, v. 21, no. 4, p. 412-422.
- Lavé, J., and Avouac, J. P., 2000, Active folding of fluvial terraces across the Siwaliks Hills, Himalayas of central Nepal: Journal of Geophysical Research, v. 105, no. B3, p. 5735-5770.
- Marshak, S., and Mitra, G., 1988, Basic methods of structural geology, USA.
- Medwedeff, D. A., 1992, Geometry and Kinematics of an active, laterally propagating wedge thrust, Wheeler Ridge, California, in Mitra, S., and Fisher, G. W., eds., Structural Geology of Fold and Thrust Belts, John Hopkins University Press, p. 3-28.
- Mitra, S., 1990, Fault-propagation folds: geometry, kinematic evolution, and hydrocarbon traps: AAPG BULLETIN, v. 74, no. 6, p. 921-945.
- -, 2002, Structural models of faulted detachment folds: AAPG BULLETIN, v. 86, no. 9, p. 1673-1694.
- Montes, C., Hatcher, R. D., and Restrepo-Pace, P. A., 2005, Tectonic reconstruction of the northern Andean blocks: Oblique convergence and rotations derived from the

kinematics of the Piedras–Girardot area, Colombia: Tectonophysics, v. 399, no. 1, p. 221-250.

- Mora, A., Gaona, T., Kley, J., Montoya, D., Parra, M., Quiroz, L. I., Reyes, G., and Strecker, M. R., 2008, The role of inherited extensional fault segmentation and linkage in contractional orogenesis: a reconstruction of Lower Cretaceous inverted rift basins in the Eastern Cordillera of Colombia: Basin Research, v. 21, no. 1, p. 111-137.
- Mora, A., Parra, M., Strecker, M. R., Sobel, E. R., Zeilinger, G., Jaramillo, C., Da Silva, S. F., and Blanco, M., 2010, The eastern foothills of the Eastern Cordillera of Colombia: An example of multiple factors controlling structural styles and active tectonics: Geological Society of America Bulletin, v. 122, no. 11-12, p. 1846-1864.
- Parra, M., Mora, A., Sobel, E. R., Strecker, M. R., and González, R., 2009, Episodic orogenic front migration in the northern Andes: Constraints from low-temperature thermochronology in the Eastern Cordillera, Colombia: Tectonics, v. 28, no. 4, p. TC4004.

- Pérez, O. J., Bilham, R., Sequera, M., Molina, L., Gavotti, P., Moncayo, C., Rodríguez, C., Guzmán, M., Codallo, H., and Velandia, R., 2011, Campo de velocidades GPS en el occidente de Venezuela: componente lateral derecha asociada a la Falla de Boconó y componente convergente perpendicular a Los Andes: Interciencia, no. 1, p. 39-44.
- Rabus, B., Eineder, M., Roth, A., and Bamler, R., 2003, The shuttle radar topography mission—a new class of digital elevation models acquired by spaceborne radar: ISPRS Journal of Photogrammetry and Remote Sensing, v. 57, no. 4, p. 241-262.

- Ramón, J., Dzou, L., Hughes, W., and Holba, A., 2001, Evolution of the Cretaceous organic facies in Colombia: implications for oil composition: Journal of South American Earth Sciences, v. 14, no. 1, p. 31-50.
- Ramon, J. C., and Fajardo, A., 2006, Sedimentology, sequence stratigraphy, and reservoir architecture of the Eocene Mirador Formation, Cupiagua field, Llanos foothills, Colombia: MEMOIRS-AMERICAN ASSOCIATION OF PETROLEUM GEOLOGISTS, v. 88, p. 433.
- Sánchez, J., Horton, B. K., Tesón, E., Mora, A., Ketcham, R. A., and Stockli, D. F., 2012, Kinematic evolution of Andean fold-thrust structures along the boundary between the Eastern Cordillera and Middle Magdalena Valley basin, Colombia: Tectonics, v. 31, no. 3, p. TC3008.
- Sarmiento, L., 2001, Mesozoic Rifting and Cenozoic INversion of the Eastern Cordillera, Colombian Andes [PhD: Vrije Universiteit Amsterdam, 295 p.
- Scharer, K., Burbank, D., Chen, J., Weldon, R., Rubin, C., Zhao, R., and Shen, J., 2004, Detachment folding in the Southwestern Tian Shan-Tarim foreland, China: shortening estimates and rates: Journal of Structural Geology, v. 26, no. 11, p. 2119-2137.
- Suppe, J., 1983, Geometry and kinematics of fault-bend folding: American Journal of science, v. 283, no. 7, p. 684-721.
- Suppe, J., and Medwedeff, D. A., 1990, Geometry and kinematics of fault-propagation folding: Eclogae geologicae Helvetiae, v. 83, no. 3, p. 409-453.

- Taboada, A., Rivera, L. A., Fuenzalida, A., Cisternas, A., Philip, H., Bijwaard, H., Olaya, J., and Rivera, C., 2000, Geodynamics of the northern Andes: Subductions and intracontinental deformation (Colombia): Tectonics, v. 19, no. 5, p. 787-813.
- Toro, J., Roure, F., Bordas-Le Floch, N., Le Cornec-Lance, S., and Sassi, W., 2004a, Thermal and kinematic evolution of the Eastern Cordillera fold and thrust belt, Colombia: Deformation, Fluid Flow, and Reservoir Appraisal in Foreland Fold and Thrust Belts: American Association of Petroleum Geologists Hedberg Series, v. 1, p. 79-115.
- -, 2004b, Thermal and kinematic evolution of the Eastern Cordillera fold and thrust belt, Colombia.
- Trenkamp, R., Kellogg, J. N., Freymueller, J. T., and Mora, H. P., 2002, Wide plate margin deformation, southern Central America and northwestern South America, CASA GPS observations: Journal of South American Earth Sciences, v. 15, no. 2, p. 157-171.
- Veloza, G., Styron, R., Taylor, M., and Mora, A., 2012, Open source archive of active faults for northwest South America: GSA Today, v. 22, no. 10, p. 4-10.
- Villamil, T., 2003, Regional hydrocarbon systems of Colombia and western Venezuela: Their origin, potential, and exploration: The Circum-Gulf of Mexico and the Caribbean: Hydrocarbon habitats, basin formation, and plate tectonics: AAPG Memoir, v. 79, p. 697-734.
- Wiltschko, D., and Chapple, W., 1977, Flow of weak rocks in Appalachian Plateau folds: AAPG BULLETIN, v. 61, no. 5, p. 653-670.

- Wiltschko, D. V., and Groshong, R. H., 2012, The Chamberlin 1910 balanced section: context, contribution, and critical reassessment: Journal of Structural Geology, v. 41, p. 7-23.

**FIGURES**

**Figure 2.1**

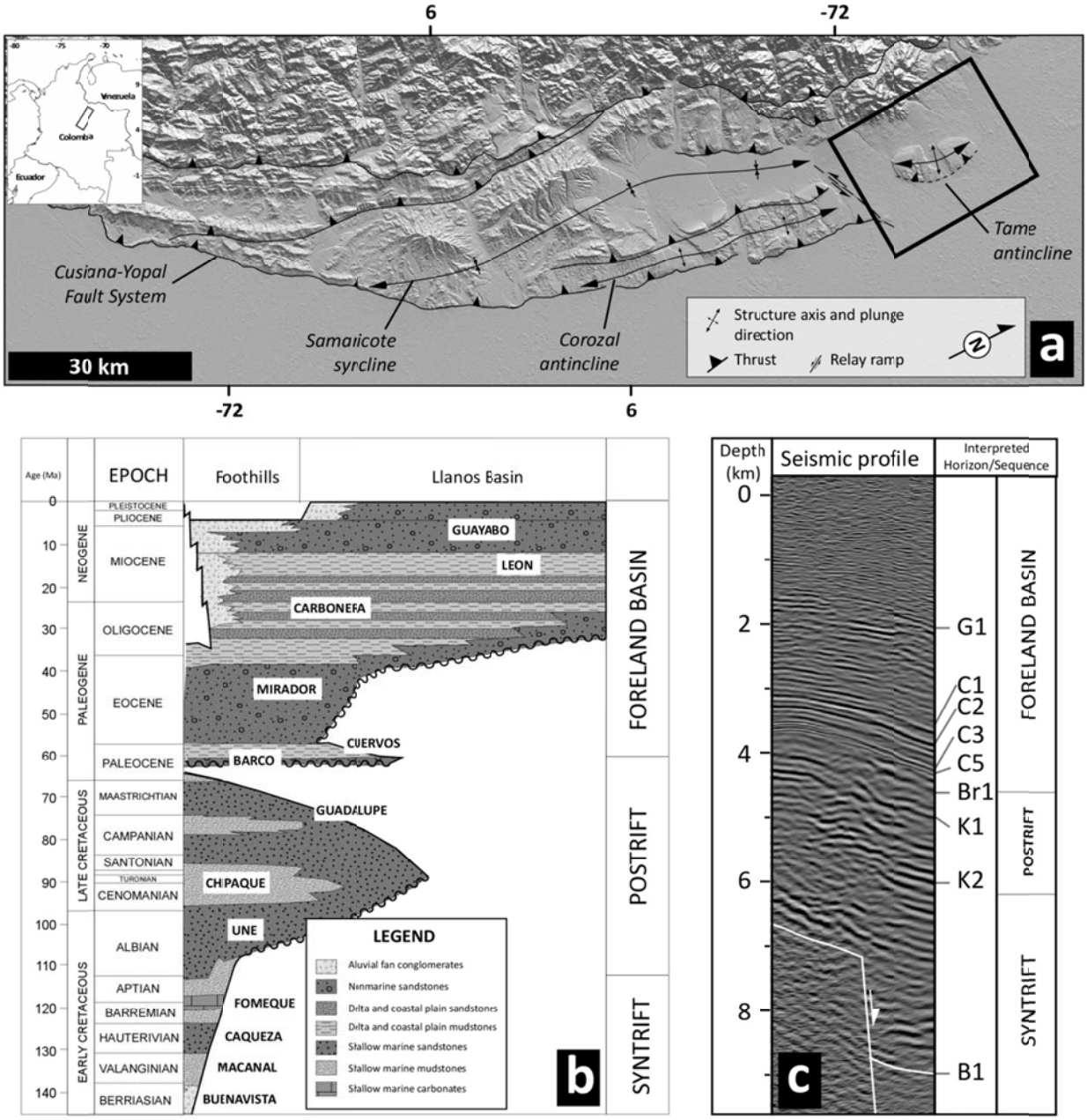

**Figure 2.1** (a) Simplified map of the active structures of the eastern foothills of the Eastern Cordillera of Colombia. Rectangle in the inset map shows the location of (a). Black box marks the location of the Tame anticline (Figure 2). (b) Generalized stratigraphic column of the eastern foothills of the Eastern Cordillera and the Llanos basin (Modified after Mora et al., 2006 and Parra et al., 2009). (c) Depth converted seismic reflection profile showing the acoustic characteristics and average depths and thicknesses of the interpreted horizons. B1: Crystalline basement. K2: Pre Une. K1: Une Fm. Br1: Barco Formation. C1-C5: Carbonera Formation. G1: Intra-Guayabo Fm.

**Figure 2.2**

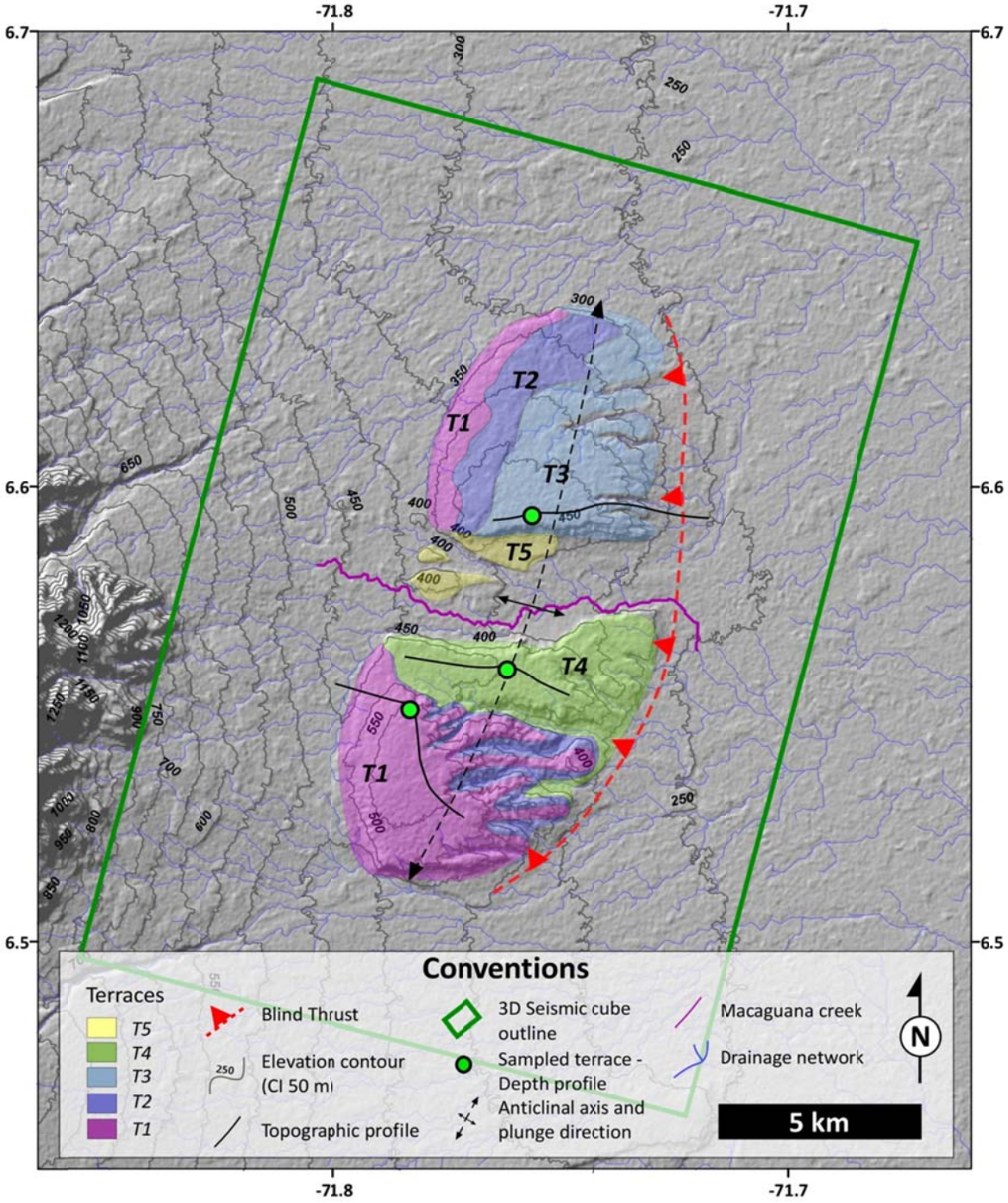
-71.8
-71.7
6.7
6.6
6.5
T1
T2
T3
T4
T5
Conventions
Terraces
T5
T4
T3
T2
T1
Blind Thrust
Elevation contour (CI 50 m
Topographic profile
3D Seismic cube outline
Sampled terrace - Depth profile
Anticlinal axis and plunge direction
Macaguana creek
Drainage network
N
5 km

**Figure 2.2** Geomorphic and neotectonic map of the Tame anticline showing uplifted, incised, and warped fluvial and alluvial deposits, and fold axes. Shaded relief map is generated from the 30 m digital elevation model (DEM) acquired during the Shuttle Radar Topography Mission (SRTM).

**Figure 2.3**

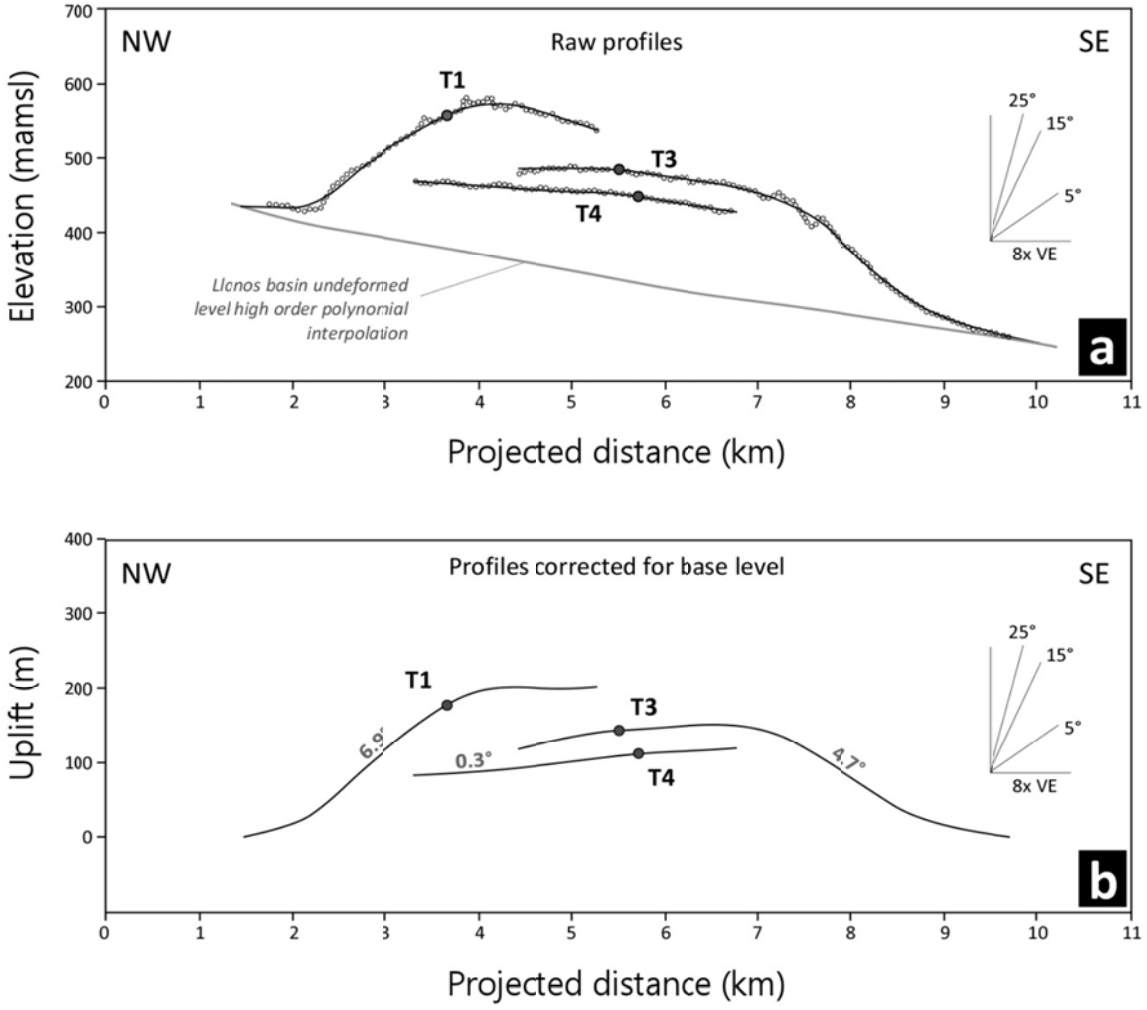
NW
Raw profiles
SE
T1
T3
T4
25°
15°
5°
8x VE
Llanos basin undeformed level high order polynomial interpolation
a
Elevation (mamsl)
Projected distance (km)
NW
Profiles corrected for base level
SE
T1
T3
T4
6.9°
0.3°
4.7°
25°
15°
5°
8x VE
b
Uplift (m)
Projected distance (km)

**Figure 2.3** Tame anticline terrace profiles. Terraces are numbered from older to younger. Filled dots indicate the location of the depth profiles within each terrace level. Location of the terrace profiles are shown on Figure 2. (a) Raw survey projected perpendicular to the fold axis profile. (b) Net incision of the fluvial terraces relative to the linear interpolation of the Llanos basin surface slope.

**Figure 2.4**

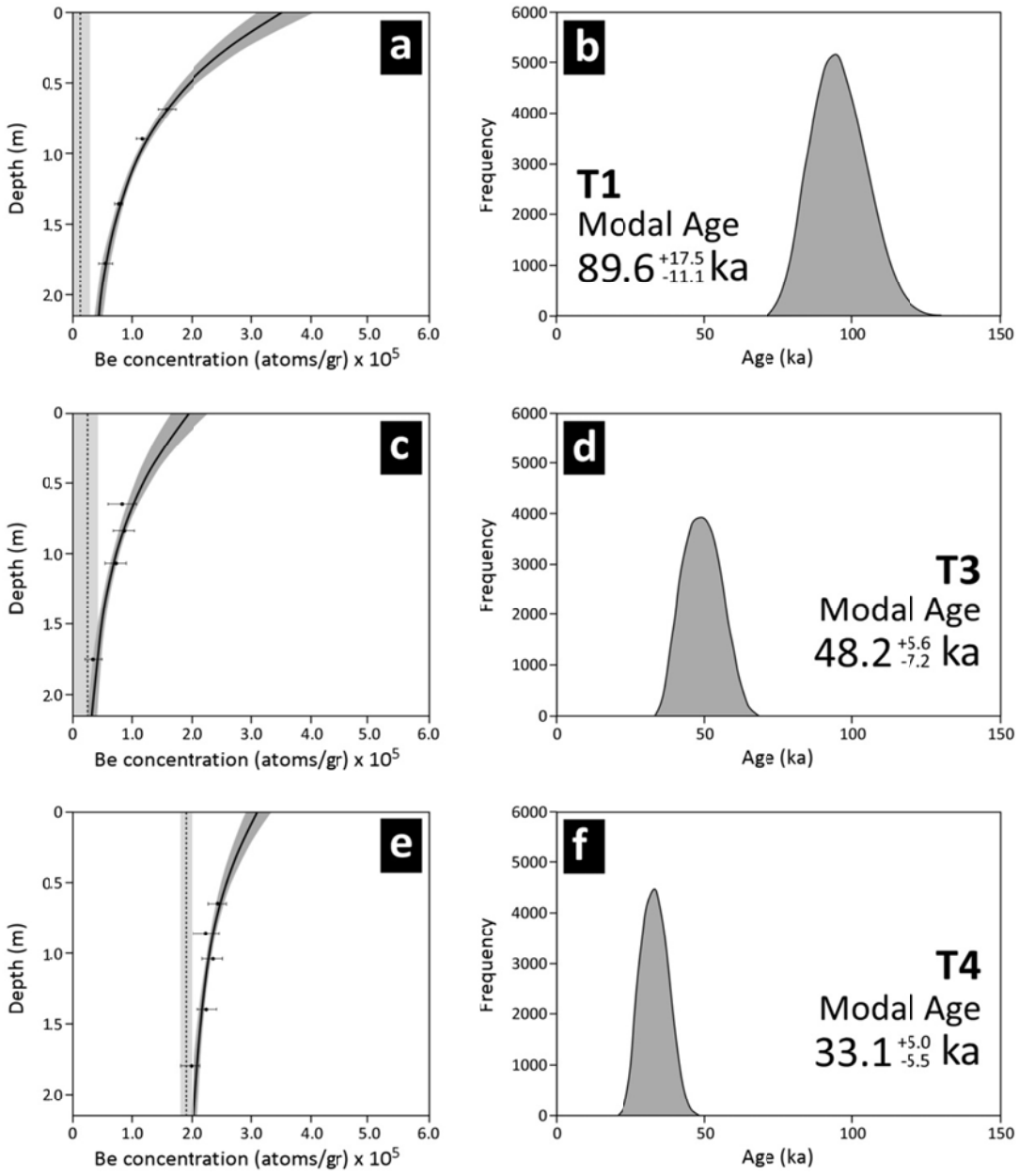
a
Depth (m)
Be concentration (atoms/gr) x 10^5
b
Frequency
T1
Modal Age
89.6 +17.5 -11.1 ka
Age (ka)
c
Depth (m)
Be concentration (atoms/gr) x 10^5
d
Frequency
T3
Modal Age
48.2 +5.6 -7.2 ka
Age (ka)
e
Depth (m)
Be concentration (atoms/gr) x 10^5
f
Frequency
T4
Modal Age
33.1 +5.0 -5.5 ka
Age (ka)

**Figure 2.4** $^{10}$Beryllium concentration versus depth profiles of the T1 (a), T3 (c) and T4 (e) terraces. Dark shaded area represents the space solution for age after 100,000 iterations of the Monte Carlo simulation (Hidy et al., 2010) and continuous line within it represents the best fit to age equation. Light shaded areas represent the 2σ error level inheritance calculation and black dotted line is the modal value. Error bars on concentration measurements are at the 2 σ error level. Age distribution histograms of the sampled terraces T1 (b), T3 (d) and T4 (f). Note that reported errors are at 1σ, while gray shaded areas represent 2σ error levels.

**Figure 2.5**

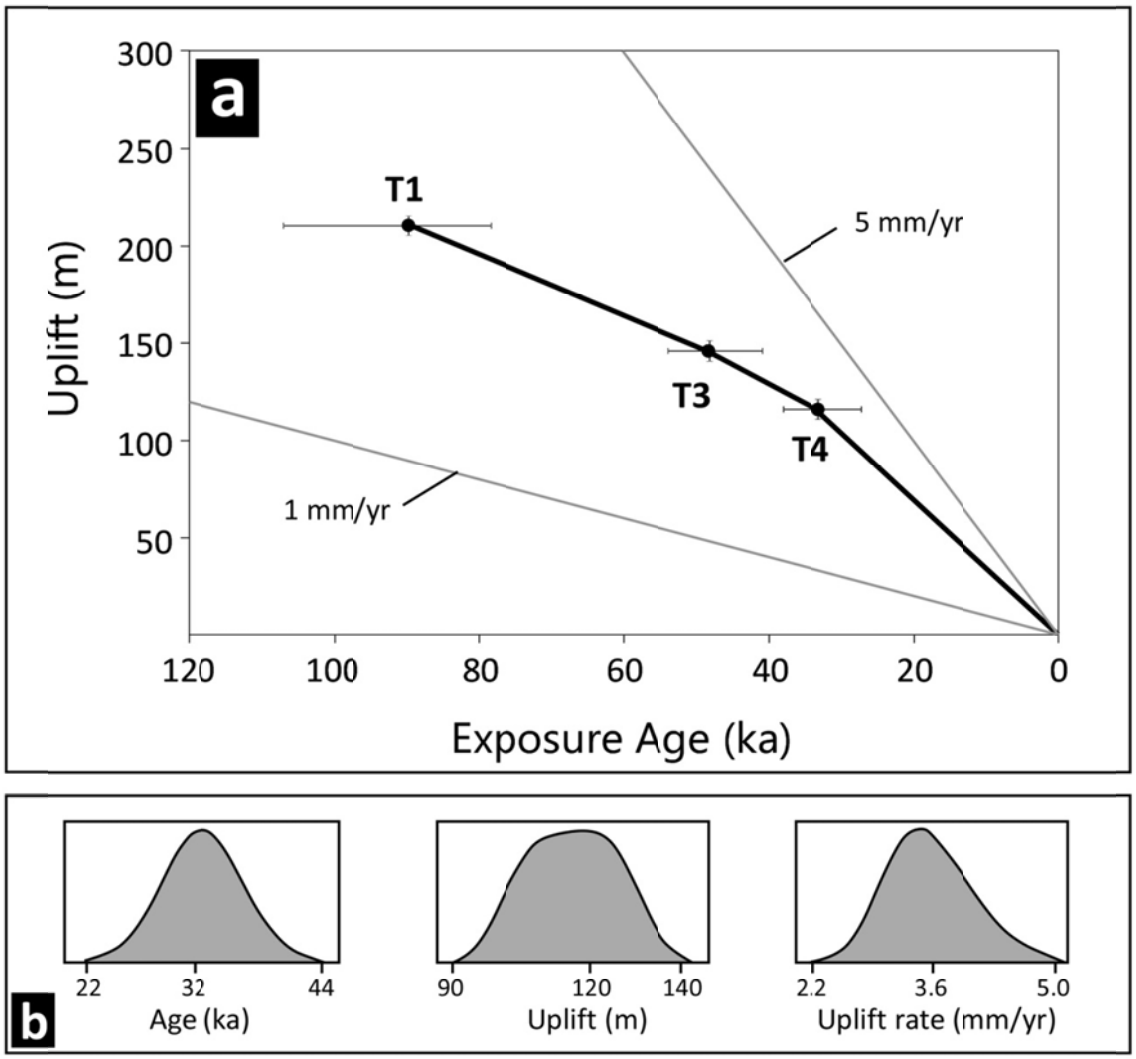
a
300
250
200
150
100
50
Uplift (m)
T1
T3
T4
5 mm/yr
1 mm/yr
120
100
80
60
40
20
0
Exposure Age (ka)
b
22
32
44
Age (ka)
90
120
140
Uplift (m)
2.2
3.6
5.0
Uplift rate (mm/yr)

**Figure 2.5** (a) Maximum uplift versus exposure age plot, showing an approximately linear trend of uplift rate of about 2.8 mm/yr. 1 mm/yr and 5 mm/yr bounds are included for reference. (b) Illustrates the methodology used to calculate the Monte Carlo simulation of the uplift rates and associated uncertainties for T4.

**Figure 2.6**

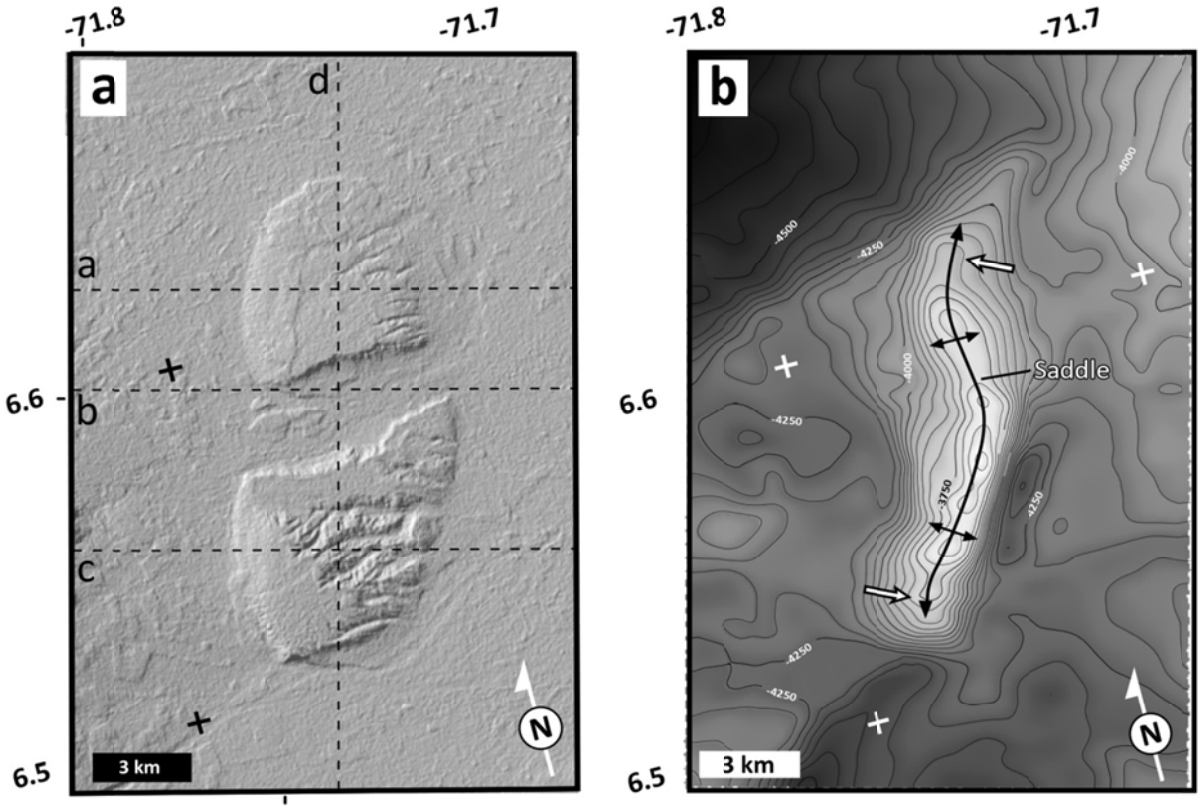

**Figure 2.6** (a) Hillshade relief map of the Tame anticline. The figure border represents outlines the 3D seismic volume analyzed in this study, and the black dotted lines represent the location of the cross sections and along-strike section for Figure 7. (b) Structural contour map of horizon C5 in meters below mean sea level (CI 50 m). Color scheme is shallower to deeper, from white to black, respectively associated with the crest of the fold. Note the change in strike and fold vergence along the fold crest, verging toward the west in the north, and towards the east in the south based on limb steepness (white arrows point in direction of fold vergence) and also the location of the saddle, that is at the same position of the saddle in the surface.

**Figure 2.7**

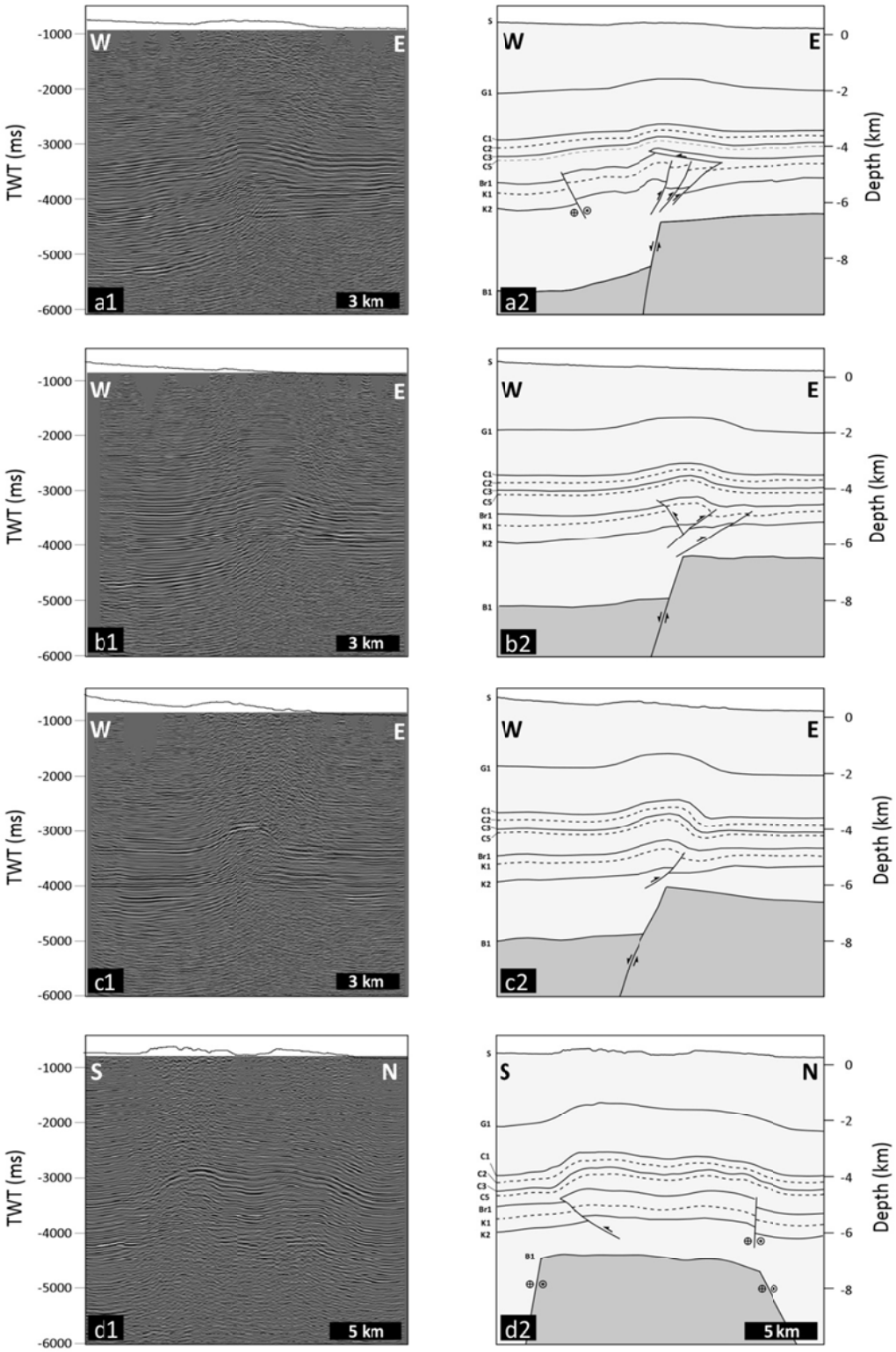
TWT (ms)
-1000
-2000
-3000
-4000
-5000
-6000
W
E
S
N
a1
b1
c1
d1
3 km
5 km
Depth (km)
0
-2
-4
-6
-8
S
G1
C1
C2
C3
C5
Br1
K1
K2
B1
a2
b2
c2
d2

**Figure 7** Representative seismic sections oriented perpendicular to the fold trend (a1, b1, c1), and an along-strike section (d1) of the Tame anticline illustrating changes in fold geometry and vergence. Seismic interpretations are shown in a2, b2, c2, d2. Depth conversion is based on interval velocities from an adjacent well within the seismic volume. See Figure 6 for location of seismic reflection profile.

**Figure 2.8**

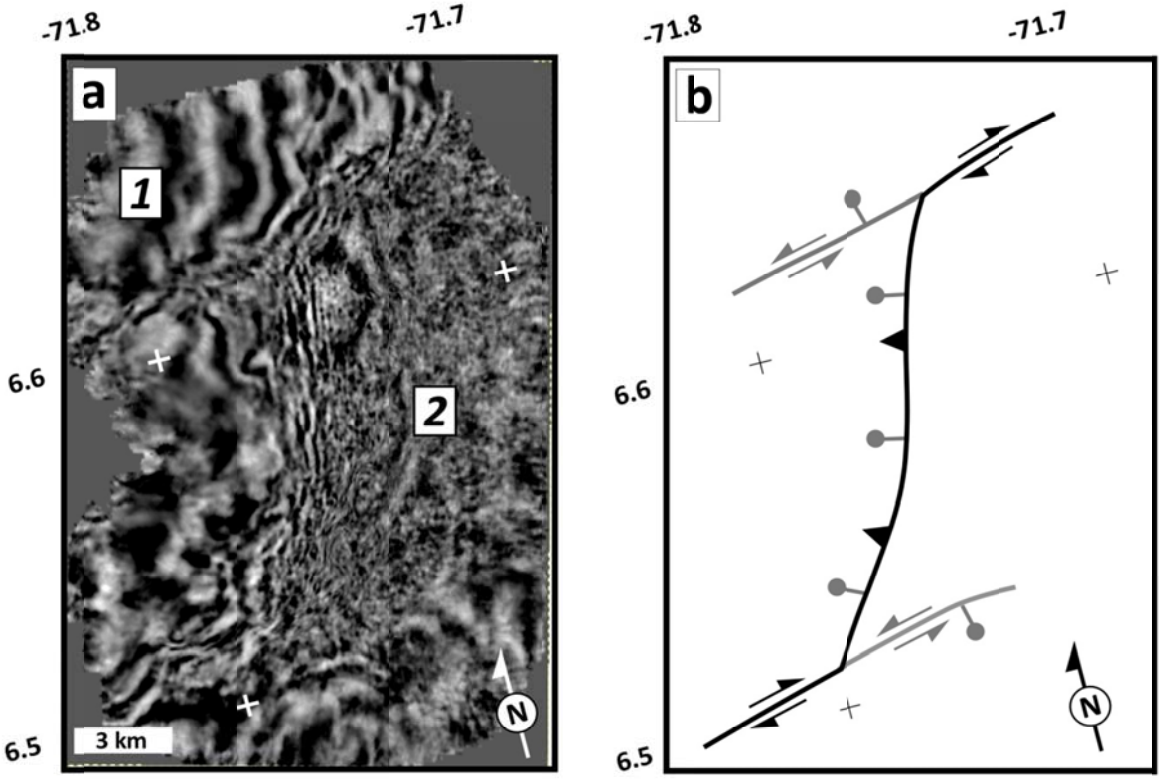

**Figure2.8** (a) Depth slice at 7.4 km depth of the depth-converted seismic survey, illustrating the change in reflectivity between the sedimentary cover (Labeled 1 on the figure) and the crystalline basement (2 on the figure). Note the continuity of the west-dipping reflectors within the sedimentary sequence in contrast to the chaotic reflections associated with the crystalline basement. (b) A schematic structural model of the west-dipping normal fault beneath the Tame anticline during the Mesozoic rifting (gray symbols) and during Quaternary contraction (black symbols). Note the coincidence of the fold terminations on the surface and in the mapped horizons.

**Figure 2.9**

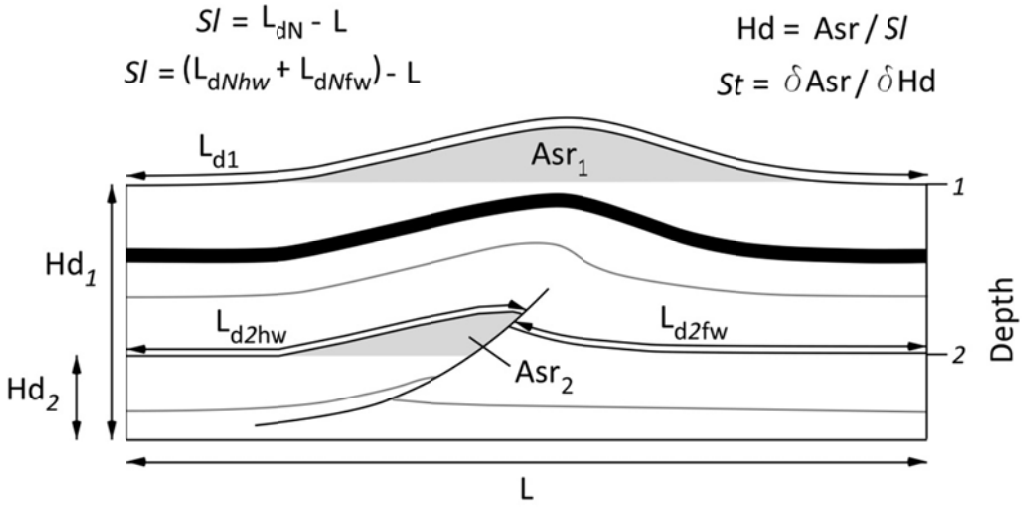
Sl = L_dN - L
Sl = (L_dNhw + L_dNfw) - L
Hd = Asr / Sl
St = δAsr / δHd
L_d1
Asr_1
1
Hd_1
L_d2hw
L_d2fw
Asr_2
2
Hd_2
Depth
L

**Figure 2.9** Schematic diagram of the methodologies used to calculate finite shortening. $Sl$: line-length shortening, that is calculated as the difference from the deformed length (Ld) and the length of the section (L). $St$: shortening as a function of depth to a reference level. St is calculated from the slope of the linear regression of area of structural relief ($Asr$) of each particular horizon and the depth to a certain reference level ($Hd$) (Epard and Groshong, 1993; Gonzalez-Mieres and Suppe, 2006).

**Figure 2.10**

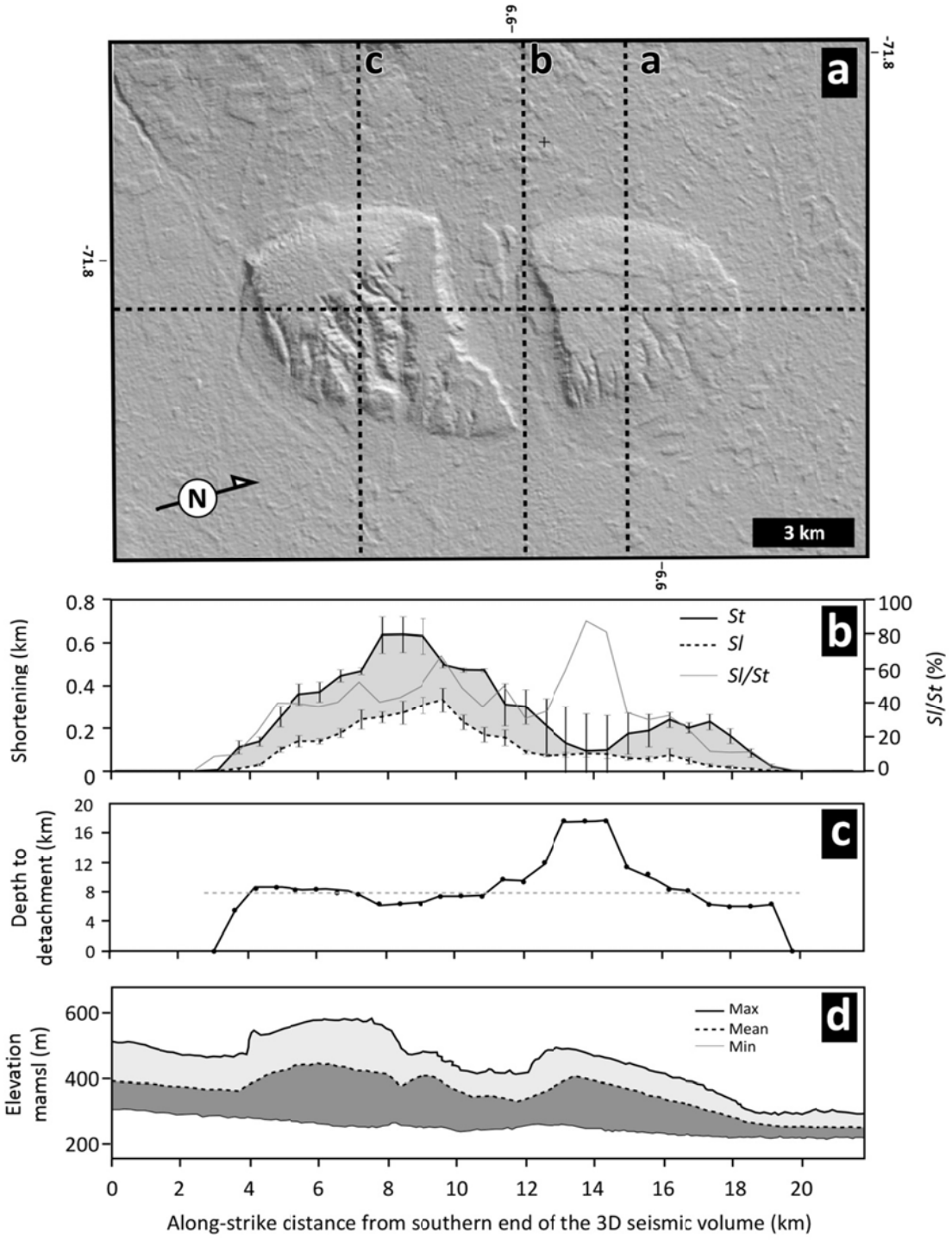
-6.6
-71.8
c
b
a
a
N
3 km
-6.9
-71.8
Shortening (km)
0.8
0.6
0.4
0.2
0
St
Sl
Sl/St
b
100
80
60
40
20
0
Sl/St (%)
Depth to detachment (km)
20
16
12
8
4
0
c
Elevation mamsl (m)
600
400
200
Max
Mean
Min
d
0
2
4
6
8
10
12
14
16
18
20
Along-strike cistance from southern end of the 3D seismic volume (km)

**Figure 2.10** (a) Hillshade map view of the Tame anticline. Dotted lines represent location of cross sections and along-strike section on Figure 7. (b) Along-strike projection of the different estimates of shortening. Shaded region represents the internal strain ($e$) obtained as the difference between finite shortening ($St$) and line-length shortening ($Sl$) (c) Calculated depth to detachment for each balanced cross section. The dotted horizontal line represents the mean depth to detachment. (d) Longitudinal topographic swath profile over the entire Tame anticline.

**Figure 2.11**

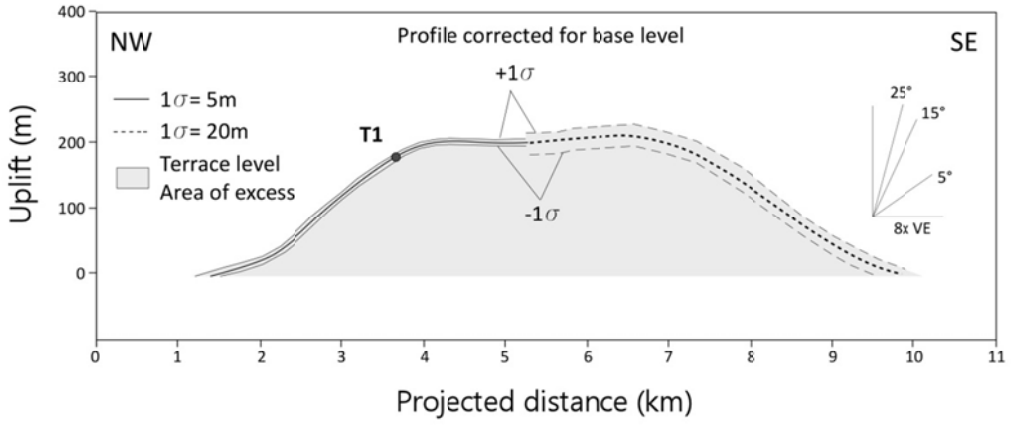
NW
Profile corrected for base level
SE
+1σ
1σ= 5m
1σ= 20m
Terrace level
Area of excess
T1
-1σ
25°
15°
5°
8x VE
Uplift (m)
Projected distance (km)
400
300
200
100
0
0
1
2
3
4
5
6
7
8
9
10
11

**Figure 2.11** Schematic diagrams showing the methodology used to estimate the topographic excess area for calculating Quaternary shortening rates for the T1 terrace. Dotted lines represent the higher order polynomial interpolation to project the pre-deformation geometry of the T1 terrace, following the overall geometry of the fold. 1 σ of the area of the profile that elevation control from the DEM is 5m (continuous line). 1 σ of the extrapolated area of the profile is 15m (dotted line).

**Table 1**

| **Table 1.** | | | | | | | | | | |
|---|---|---|---|---|---|---|---|---|---|---|
| Sample | Depth (cm) | Thickness (cm) | Quartz (g) | Be Carrier (mg)[a,b] | $^{10}Be/^{9}Be$ ($\times 10^{-13}$) | | | $^{10}Be$ Concentra tiong ($10^4$ atoms $g^{-1}$ $SiO_2$) | | |
| 1 | 175 | 12 | 44.65 | 0.3033 | 0.898 | ± | 0.080 | 3.710 | ± | 0.370 |
| 2 | 133 | 6 | 49.25 | 0.2972 | 2.318 | ± | 0.099 | 8.891 | ± | 0.401 |
| 3 | 107 | 7 | 65.68 | 0.2778 | 2.714 | ± | 0.124 | 7.312 | ± | 0.351 |
| 4 | 84 | 8 | 51.49 | 0.3017 | 2.387 | ± | 0.100 | 8.898 | ± | 0.394 |
| 5 | 65 | 5 | 51.13 | 0.2893 | 2.466 | ± | 0.110 | 8.878 | ± | 0.416 |
| 6 | 180 | 5 | 37.39 | 0.3052 | 3.758 | ± | 0.096 | 19.709 | ± | 0.526 |
| 7 | 140 | 7 | 48.27 | 0.2820 | 6.421 | ± | 0.340 | 24.256 | ± | 1.303 |
| 8 | 104 | 6 | 49.80 | 0.2657 | 6.515 | ± | 0.231 | 22.469 | ± | 0.812 |
| 9 | 86 | 4 | 44.42 | 0.2965 | 5.214 | ± | 0.208 | 22.460 | ± | 0.914 |
| 10 | 65 | 5 | 55.99 | 0.3099 | 6.684 | ± | 0.153 | 23.950 | ± | 0.560 |
| 11 | 190 | 5 | 41.66 | 0.2904 | 1.339 | ± | 0.075 | 5.803 | ± | 0.360 |
| 12 | 145 | 5 | 70.24 | 0.3112 | 2.713 | ± | 0.088 | 7.679 | ± | 0.263 |
| 13 | 114 | 4 | 68.79 | 0.2904 | 2.250 | ± | 0.106 | 6.027 | ± | 0.300 |
| 14 | 96 | 4 | 67.56 | 0.3192 | 3.754 | ± | 0.110 | 11.406 | ± | 0.347 |
| 15 | 73 | 4 | 50.95 | 0.2998 | 4.170 | ± | 0.132 | 15.793 | ± | 0.515 |
| [a] Carrier concentration 1522 ppm | | | | | | | | | | |
| [b] Carrier density 1.0228 g/ml | | | | | | | | | | |

**Table 1** Summary of sample TCN data from the Tame anticline using guidelines from Frankel et al. (2010).

**Table 2**

| Table 2 | | | | | | | | | | |
|---|---|---|---|---|---|---|---|---|---|---|
| Terrace | Lat | Long | Elevation (m above sea level) | Samples | Production Rate (atoms g -1 yr -1 ) | Denudation Rate (mm yr -1 ) | Modal inheritance ($10^{4}$ atoms g–1) | Modal age (ka) | Age Maximum (ka) | Minimum Age (ka) |
| T1 | 6.5516 | -71.7825 | 554 | 11 - 15 | 3.97 | 0.27 | 1.22 | 89.6 | 124.6 | 71.2 |
| T3 | 6.5914 | -71.7565 | 501 | 1 - 5 | 3.82 | 0.09 | 1.18 | 48.2 | 59.4 | 33.8 |
| T4 | 6.5607 | -71.7617 | 454 | 6 - 10 | 3.69 | 0.46 | 19.7 | 33.1 | 43.1 | 22.2 |

**Table 2** Statistics for the Monte Carlo simulations of three depth profiles from the Tame anticline. Maximum and minimum values represent the 95% (2σ) confidence window for each parameter.